Materials Today Bio 25 (2024) 100959

Contents lists available at ScienceDirect

Materials Today Bio

journal homepage: www.journals.elsevier.com/materials-today-bio

Incorporating strontium enriched amorphous calcium phosphate granules in collagen/collagen-magnesium-hydroxyapatite osteochondral scaffolds improves subchondral bone repair

Jietao Xu [a,1], Jana Vecstaudza [b,1], Marinus A. Wesdorp [a], Margot Labberté [c], Nicole Kops [a], Manuela Salerno [d], Joeri Kok [e], Marina Simon [f], Marie-Françoise Harmand [f], Karin Vancíková [c], Bert van Rietbergen [e], Massimiliano Maraglino Misciagna [g], Laura Dolcini [g], Giuseppe Filardo [d], Eric Farrell [h], Gerjo J.V.M. van Osch [a,i,j], Janis Locs [b,k,**,2], Pieter A.J. Brama [c,*,2]

[a] Department of Orthopedics and Sports Medicine, Erasmus MC, University Medical Center Rotterdam, Rotterdam, 3015 GD, Netherlands
[b] Rudolfs Cimdins Riga Biomaterials Innovations and Development Centre of RTU, Institute of General Chemical Engineering, Faculty of Materials Science and Applied Chemistry, Riga Technical University, LV-1007, Riga, Latvia
[c] School of Veterinary Medicine, University College Dublin, Dublin, D04 W6F6, Ireland
[d] Applied and Translational Research Center, IRCCS Rizzoli Orthopaedic Institute, Bologna, 40136, Italy
[e] Department of Biomedical Engineering, Eindhoven University of Technology, Eindhoven, 5612 AZ, Netherlands
[f] Groupe ICARE, Martillac, 33650, France
[g] Fin-Ceramica Faenza S.p.A, Faenza, 48018, Italy
[h] Department of Oral and Maxillofacial Surgery, Erasmus MC, University Medical Center Rotterdam, Rotterdam, 3015 GD, Netherlands
[i] Department of Otorhinolaryngology, Head and Neck Surgery, Erasmus MC, University Medical Center Rotterdam, Rotterdam, 3015 GD, Netherlands
[j] Department of Biomechanical Engineering, Delft University of Technology, Delft, 2628 CD, Netherlands
[k] Baltic Biomaterials Centre of Excellence, Headquarters at Riga Technical University, LV-1048, Riga, Latvia

ARTICLE INFO

Keywords:
Tissue engineering
Regenerative medicine
Osteochondral defect
Amorphous calcium phosphate
Strontium

ABSTRACT

Osteochondral defect repair with a collagen/collagen-magnesium-hydroxyapatite (Col/Col-Mg-HAp) scaffold has demonstrated good clinical results. However, subchondral bone repair remained suboptimal, potentially leading to damage to the regenerated overlying neocartilage. This study aimed to improve the bone repair potential of this scaffold by incorporating newly developed strontium (Sr) ion enriched amorphous calcium phosphate (Sr-ACP) granules (100–150 μm). Sr concentration of Sr-ACP was determined with ICP-MS at 2.49 ± 0.04 wt%. Then 30 wt% ACP or Sr-ACP granules were integrated into the scaffold prototypes. The ACP or Sr-ACP granules were well embedded and distributed in the collagen matrix demonstrated by micro-CT and scanning electron microscopy/energy dispersive x-ray spectrometry. Good cytocompatibility of ACP/Sr-ACP granules and ACP/Sr-ACP enriched scaffolds was confirmed with *in vitro* cytotoxicity assays. An overall promising early tissue response and good biocompatibility of ACP and Sr-ACP enriched scaffolds were demonstrated in a subcutaneous mouse model. In a goat osteochondral defect model, significantly more bone was observed at 6 months with the treatment of Sr-ACP enriched scaffolds compared to scaffold-only, in particular in the weight-bearing femoral condyle subchondral bone defect. Overall, the incorporation of osteogenic Sr-ACP granules in Col/Col-Mg-HAp scaffolds showed to be a feasible and promising strategy to improve subchondral bone repair.

* Corresponding author.
** Corresponding author. Rudolfs Cimdins Riga Biomaterials Innovations and Development Centre of RTU, Institute of General Chemical Engineering, Faculty of Materials Science and Applied Chemistry, Riga Technical University, LV-1007, Riga, Latvia.
E-mail addresses: janis.locs@rtu.lv (J. Locs), pieter.brama@ucd.ie (P.A.J. Brama).
[1] Authors contributed equally.
[2] Corresponding authors contributed equally.

https://doi.org/10.1016/j.mtbio.2024.100959
Received 28 September 2023; Received in revised form 10 January 2024; Accepted 15 January 2024
Available online 20 January 2024

1. Introduction

Pain and restriction-free movement of joints is possible when the osteochondral unit is well preserved. The native osteochondral unit is composed of two main tissue types: articular cartilage and subchondral bone which are connected via calcified cartilage. Healthy articular cartilage ensures joint lubrication and stress reduction, and the subchondral bone is crucial for underlying mechanical support. These functions can be altered if the complex structure of the osteochondral unit is damaged by traumatic injuries, chronic diseases, and age-related degeneration. Endogenous osteochondral defect repair is limited due to the lack of a vascular/nerve supply in the cartilage and the complex multiphasic structure of the osteochondral unit [1,2]. Due to its limited self-healing capacity, osteochondral defects may progress into osteoarthritis without effective and timely intervention. To regenerate osteochondral tissue in the lesion site, surgical interventions, such as autologous chondrocyte implantation, osteochondral grafting, and microfracture have been extensively applied. Regenerated tissue, however, mainly consists of a mixture of fibrous tissue and fibrocartilage [3,4], leading to poor resistance to shear forces and deterioration at long-term follow-up [5,6].

To improve osteochondral tissue repair, biomaterial-based scaffolds have shown promising results in regenerating damaged tissues. To mimic the native osteochondral composition and structure, biomaterial-based bilayered scaffolds have been developed and tested [7]. Among these, a scaffold with a superficial collagen-only layer and a deep layer of collagen mixed with magnesium-containing hydroxyapatite (Mg-HAp) represents a promising substitute [8,9]. Each side of the scaffold provides unique chemical (e.g., biomimetic chemical composition) and physical (e.g., stiffness, elasticity) cues for chondrogenesis and osteogenesis. Specifically, collagen is a biologically derived protein and therefore an efficient biomaterial to support cellular activities and promote osteochondral repair [10]. Next, bioactive magnesium (Mg) ions have been introduced in the mineral phase of HAp to enhance the affinity of HAp with natural bone and promote an increase in cell osteogenic activity [11]. Clinically, this collagen/collagen-magnesium-hydroxyapatite (Col/Col-Mg-HAp) scaffold has demonstrated good stability and clinically relevant improvement in knee function [12–14]. However, subchondral bone repair remained suboptimal in comparison to the cartilage repair capacity of this scaffold in clinical follow-up [14]. The unrepaired subchondral bone may affect the biomechanical properties of the osteochondral unit, which might lead to damage to the regenerated overlying neocartilage and joint pain for the patient. Well-healed subchondral bone is, therefore, critical to support long-term survival of the overlying neocartilage [15].

We hypothesize that addition of extra calcium phosphate (CaP) to the Col/Col-Mg-HAp scaffold would enhance the regeneration of the subchondral bone. That extra CaP could be the well-known hydroxyapatite (HAp, $Ca_{10}(PO_4)_6(OH)_2$) which is a close chemical analogue to the biological apatite present in bone [16]. However, the stoichiometric HAp, in comparison with biological apatite, has low solubility and resorbability [17]. Limitations of HAp could be overcome by additionally using amorphous calcium phosphate (ACP). ACP is a hydrated CaP with an amorphous structure, allowing different Ca/P molar ratios (1.2–2.2), and a high specific surface area [18,19]. The presence of an amorphous phase, hydrated structure and high specific surface area of ACP are shared with the biological apatite [20], and it ensures ACP's bioactivity, solubility, and excellent adsorption properties of biologically relevant ions and molecules [18].

As ACP's amorphous structure can accommodate other ions besides calcium and phosphate [21], it can be modified to include other ions for an additional bone regenerative effect. Bioinorganic ions such as strontium (Sr) are cost-effective and easy to use as a local delivery tool [22] having less risk than bone morphogenetic protein (BMP) strategies used for improved regeneration of bone [23]. Previously Sr has been introduced in forms of a Sr ranelate drug or as a dopant in the biomaterial of choice [24–26], this includes CaPs as well. On a cellular level, Sr ions have a dual mode of action: stimulation of osteoblasts and inhibition of osteoclasts [27,28]. Sr promotes formation of extracellular matrix (ECM) proteins produced by osteoblasts [29]. These effects might be useful in repair of the subchondral bone as well. In the available studies the use of Sr containing biomaterials in bone defect repair is already well established [22,30,31] and it leads to improved or at least unchanged new bone formation compared to the Sr-free groups [32]. However, the specific effects of Sr and even ACP on subchondral bone regeneration are still yet to be provided.

In particular, the combination of a recently developed ACP with high specific surface area (>100 m^2/g) [33–36] and Sr ions might provide excellent cues for ECM formation and subchondral bone tissue regeneration through sustaining of an ion-rich microenvironment. Upon contact with the biological environment, dissolution of strontium, calcium and phosphate ions is expected, which are favouring cues for ECM production and bone formation [37]. The Sr ion effect on chondrogenesis is less studied, however, it has been found that the Sr ions upregulate cartilage-specific gene expression and thus facilitate differentiation towards chondrogenic cell lineage [38,39].

In this study, we modified the synthesis technology of ACP for incorporation of Sr, and developed a method to incorporate ACP/Sr-ACP granules into the Col/Col-Mg-HAp scaffold (upper cartilaginous layer with the average 100–150 μm pore diameter, the lower bony layer with the average 250–450 μm pore diameter [12]). Then we characterized physicochemical properties and the *in vitro* cytocompatibility of ACP or Sr-ACP granules and ACP/Sr-ACP enriched Col/Col-Mg-HAp scaffolds. To evaluate the osteogenic potential in osteochondral defects, we first investigated the biocompatibility and osteogenic effect of ACP/Sr-ACP enriched scaffold in an *in vivo* semi-orthotopic mouse model at the early phases of repair. Finally, the osteogenic effect of the Sr-ACP enriched Col/Col-Mg-HAp scaffold was investigated *in vivo* in a translational large animal (goat) osteochondral defect model.

2. Materials and methods

2.1. Synthesis of ACP and Sr-ACP

ACP and Sr-ACP granules used in the study were prepared from materials synthesized according to a wet precipitation technology developed previously [34]. Here, the synthesis technology was modified (use of calcium oxide instead of hydroxyapatite), and a novel synthesis procedure of ACP/Sr-ACP was developed as described below.

First, 2.71 g of CaO (calcined $Ca(OH)_2$ (Jost Chemical Co., USA)) and 0.438 g of $Sr(NO_3)_2$ (Sigma-Aldrich, Germany) were mixed in deionized water (300 mL). The amount of Sr within Sr-ACP was chosen to be 50x the maximum amount reported of Sr in bone mineral (0.05 wt% [40] i.e., 2.5 wt%). The mixing was done with an overhead mixer MM-1000 (Biosan, Latvia) equipped with a propeller stirrer at 300–400 rpm at 20 ± 2 °C. Then 14.48 mL of 2 M H_3PO_4 (75 %, "Latvijas Kimija" Ltd.) was admixed and the suspension was stirred for 30 min. Next, 32.3 mL 3 M HCl (Merck EMSURE®, Austria) at a rate of 5 mL/min was added. Resulting in dissolution of reagents, and thus a transparent solution containing calcium, phosphate, strontium, and nitrate ions was obtained. Next, after 30 min the mixing speed was increased to 450–550 rpm and an equimolar amount of 2 M NaOH (Merck EMSURE®, Germany) was rapidly admixed to raise the pH and to induce precipitation of Sr-ACP. Then the stirring was continued for another 5 min until the reading of the pH electrode stabilized (pH 10–11). Next, the precipitated Sr-ACP was separated by vacuum filtration. During the filtration, the Sr-ACP was washed with deionized water (1.5–2.0 L) to remove any formed water-soluble by-products, e.g., NaCl, from the precipitates. The presence of NaCl was tested by adding a few drops of 0.1 M silver nitrate to the solution that had passed the filter. When the formation of an opaque precipitate was not observed after the addition of the silver nitrate, it was considered that the solution did not contain NaCl. Then, the washed Sr-ACP was transferred onto glass Petri dishes, spread evenly,

and dried at 80 °C for 1 h in a drying oven with forced air circulation (UFE 400, Memmert, Germany). A schematic overview of the synthesis is shown in Fig. 1. Synthesis of ACP was analogous but without the addition of $Sr(NO_3)_2$.

2.2. Production and characterization of ACP and Sr-ACP granules

ACP/Sr-ACP granules were manufactured using dry granulation technology (Fig. 1) which involved milling of the synthesized ACP/Sr-ACP followed by sieving of the milled material to the desired range of granule size. In brief, the dried ACP/Sr-ACP precipitates were in the form of flat agglomerates (<3 mm thick). The agglomerates were manually crushed in a mortar and further sieved using sieves and a vibratory sieve shaker Analysette 3 (Fritsch GmbH, Germany). The sieving resulted in ACP/Sr-ACP granules in a size range of 100–150 μm. The debris that was formed during granulation was removed by rinsing the granules with ethanol (96 %). The rinsed granules were dried in a drying oven (UFE 400, Memmert, Germany) with forced air circulation at 80 °C (3 h). The manufactured ACP/Sr-ACP granules were characterized for their physicochemical properties as described below.

Phase composition of the synthesized ACP/Sr-ACP products was analysed using x-ray diffraction (XRD) with an X'Pert Pro (Malvern Panalytical B·V., The Netherlands) diffractometer. The diffractometer was equipped with a Cu tube run at 40 kV and 30 mA. In the path of diffracted x-rays, a Ni filter was installed to minimize Cu Kβ radiation. The XRD patterns were acquired in 2Theta range 10–70° with a step size of 0.0334° and time per step of 30.48 s. Powdered samples were put on a front-loading sample holder with a low background Si insert.

Information about chemical groups was gathered using a Fourier-transform infrared spectrometer (Varian 800 FT-IR, Scimitar Series, USA) in an attenuated reflectance (ATR, GladiATR™, Pike technologies, USA) mode. Samples were finely ground and analysed in the form of a powder. FT-IR spectra were obtained at 4 cm^{-1} resolution co-adding 50 scans over a range of wavenumbers from 400 cm^{-1} to 4000 cm^{-1}. Before each FT-IR measurement, a background spectrum was taken and later deducted from the sample spectrum.

Specific surface area (SSA) of the granules was determined by using an N_2 adsorption system Quadrasorb SI Kr (Quantachrome Instruments, USA) with Autosorb Degasser AD-9 (Quantachrome Instruments, USA). Samples (0.5 g, n = 3) were degassed at room temperature to remove any adsorbed volatiles. Calculation of the SSA was done according to Brunauer-Emmett-Teller (BET) theory. Next, the calculated particle size (d_{BET}) was found using the following equation: $d_{BET} = 6000/(SSA \times density)$, assuming particles to be spherical.

Granule morphology was visualized using a field emission scanning electron microscope (SEM) Mira (Tescan, Czech Republic). SEM imaging was done at an accelerating voltage of 5 kV with both scanning electron (SE) and backscattered electron (BSE) detectors. Before the SEM imaging, samples were attached to sample holders with double-sided carbon tape and then coated with a layer of gold using sputter coater K550X (Quorum technologies, UK). Sputtering parameters were 25 mA for 180 s in an argon atmosphere with a sample rotation to obtain a homogenous coating. Additionally, the scaffolds were analysed with an energy dispersive x-ray spectrometer (EDS) X-Max^N 150 (Oxford Instruments, UK) to obtain element distribution maps. To obtain element maps the electron gun was operated at 15 kV. The mapping area was selected by drawing a rectangle over the image of the sample. The EDS mapping was done with Inca software (Oxford Instruments, UK).

Strontium concentration in Sr-ACP granules was determined using an inductively coupled plasma-optical emission spectrometry (ICP-OES, Thermo Scientific iCAP 7400, Waltham, MA, USA). The sample was dissolved in nitric acid (65 v/v%). The content (ppm) in the samples was determined by comparison with a predetermined standard curve. Sr (wt %) was calculated on the basis of the sample weight.

2.3. Preparation and characterization of ACP/Sr-ACP granule containing collagen/collagen-magnesium-hydroxyapatite osteochondral scaffolds

Col/Col-Mg-HAp with/without ACP or Sr-ACP granules are biomimetic scaffolds that have a porous, 3-dimensional composite structure. The scaffold is composed of two layers: the cartilaginous layer consisting of Type I collagen and the bone layer consisting of a combination of Type I collagen (60 %) and magnesium-hydroxyapatite (40 %, Mg-HAp). Each layer of the scaffold was synthesized separately by a standardised process from an atelocollagen aqueous solution (1 wt%) in acetic acid, isolated from equine tendon. The upper non-mineralised chondral layer of the scaffold was obtained by dissolving an acetic solution of Type I collagen in bi-distilled water by adding NaOH. The bone layer of the scaffold was obtained by nucleating nanostructured Mg-HAp into self-assembling collagen fibres, as occurs in the natural biological neo-ossification process. To stabilize the scaffold, the fibrous structures were chemically cross-linked for 16 h at room temperature. After chemical cross-linking, ACP or Sr-ACP granules were added through a deposition by vacuum directly into the bone layer during the prefiltration phase. The two layers were superimposed and afterwards they are freeze-dried. Finally, the scaffolds were gamma sterilized at 25 KGy.

ACP/Sr-ACP granule integration within the Col/Col-Mg-HAp scaffolds was evaluated using SEM/EDS and micro-CT techniques. Prior SEM imaging and EDS element mapping samples were cross sectioned with a scalpel. Further, the sample preparation procedure was the same as described above for ACP/Sr-ACP granules alone (section 2.2).

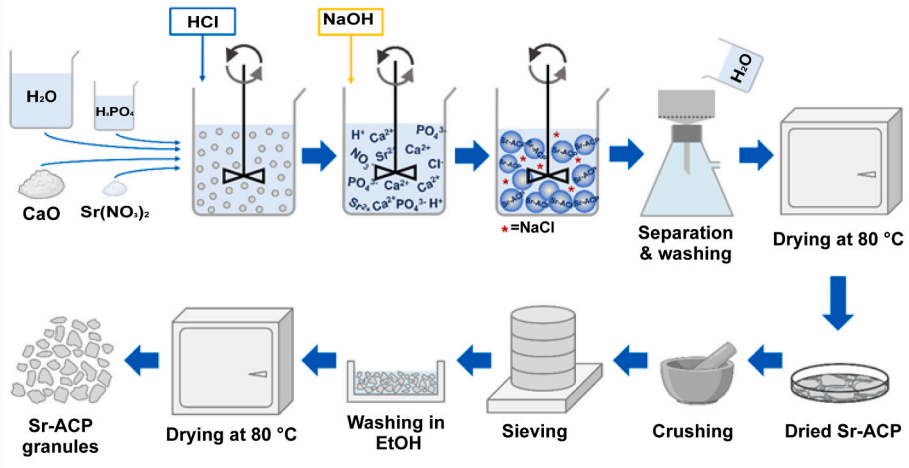

Fig. 1. Schematic overview of the Sr-ACP synthesis procedure (top) and dry granulation technology (bottom) for obtaining Sr-ACP granules.

Further micro-CT analysis of the scaffolds was performed with a micro-CT 50 instrument (Scanco Medical, Wangen-Brüttisellen, Switzerland). A sample holder with a diameter of 14 mm was used in which the scaffold was fixed with PU foam. Parameters of micro-CT control file were: energy 70 KV; intensity 114 μA; resolution - native; field of view 15.2 mm; voxel size 3.4 μm; integration time 2000 s. Scans were done under a 0.5 mm thick Al filter. The instrument was calibrated against a hydroxyapatite phantom.

2.4. *In vitro cytotoxicity*

To assess the possible cytotoxicity of the developed ACP/Sr-ACP granules and scaffolds, the *in vitro* cell viability was assessed. Granules or scaffolds were incubated in Dulbecco's Modified Eagle Medium high glucose (DMEM, high glucose, Gibco, Waltham, MA, USA) supplemented with 10 % fetal bovine serum (FBS, Gibco, Waltham, MA, USA) under gentle agitation for 24 h at 37 °C to obtain extracts. An extraction ratio of 0.2 g/mL for granules and 3 cm^2/mL for scaffolds was considered, according to ISO 10993–12. Balb/c 3T3 clone A31 were seeded at 15,000 cells/cm^2 then incubated for 24 h at 37 °C before exposition to the extracts. 30 % Sr-ACP/Sr-ACP granules (in weight of the scaffold) will be incorporated into the scaffold. And 30 % Sr-ACP/Sr-ACP granules in weight of the scaffold are equivalent to 8 % ACP or Sr-ACP extract dilutions. Therefore, cells were incubated in culture medium with ACP or Sr-ACP extracts (25 % and successive dilutions 15 %, 8 % and 2.5 %) or scaffold extracts (100 % and successive dilutions 40 %, 16 % and 6.4 %) for 48 h at 37 °C in a humidified atmosphere with 5 % CO_2. Negative control (complete culture medium) and positive control for cytotoxicity (Phenol) were run in parallel. At the end of the incubation period, culture medium was removed and discarded. Cells were detached using trypsin solution. Then, a Trypan Blue solution with 10 % FBS was added. Living cells were counted using a haemocytometer.

2.5. *In vivo osteochondral defect mice model*

To evaluate the biocompatibility and osteogenic capacity of ACP/Sr-ACP granules incorporated into the Col/Col-Mg-HAp scaffold *in vivo*, a semi-orthotopic osteochondral defect model established by our group was used (Fig. 2A) [41]. In order to model several larger critical sized bone defects using a small animal model, we created a semi-orthotopic osteochondral defect model by implanting bovine osteochondral explants subcutaneously in mice. Briefly, osteochondral defects (4 mm in diameter, 4 mm in depth) were created in the explants (8 mm in diameter, 5 mm in height) harvested from metacarpal-phalangeal joints of 6–8 months old calves (LifeTec, Eindhoven, The Netherlands) with a hand drill. The osteochondral explants were cultured overnight in alpha-Minimum Essential Medium (α-MEM; Gibco, Massachusetts, USA) supplemented with 10 % fetal bovine serum (FBS, Gibco, Massachusetts, USA), 50 μg/mL gentamycin (Gibco, Massachusetts, USA), and 1.5 μg/mL fungizone (Gibco, Massachusetts, USA). Then the osteochondral defects were fitted with: (1) Col/Col-Mg-HAp scaffold-only (n = 6, osteochondral scaffold, Finceramica, Italy, diameter: 4 mm, height: 4 mm), or (2) ACP enriched Col/Col-Mg-HAp scaffold (n = 7), or (3) Sr-ACP enriched Col/Col-Mg-HAp scaffold (n = 7). All osteochondral explants were covered with a circular 8 mm Neuro-Patch membrane (Braun, Melsungen, Germany) to prevent the ingrowth of host cells from the top.

Five 12-week-old NMRI-Fox1nu female mice (Taconic, New York, USA) were randomly assigned and housed under specific-pathogen-free conditions with a regular day/night light cycle. Food and water were available ad libitum. The mice were allowed to adapt to the conditions of the animal facility for 7 days. The osteochondral explants were implanted subcutaneously on the back of the mice under 2.5–3% isoflurane anesthesia (1000 mg/g, Laboratorios Karizoo, Maharashtra, India). 4 osteochondral explants were implanted in 4 pockets per mouse respectively. Staples (Fine Science Tools, Vancouver, Canada) were used to close the incisions and were removed 1 week after implantation. To ensure pre- and post-operative analgesia, the mice received a subcutaneous injection of 0.05 mg/kg bodyweight of buprenorphine (Ividior, North Chesterfield, Virginia, USA) 1 h before surgery and 6–8 h after surgery. Mice received a subcutaneous prophylactic antibiotic injection of 25 mg/kg body weight of Amoxicillin (Dopharma, Raamsdonksveer, Netherlands).

After 8 weeks, mice were euthanized by cervical dislocation under 2.5–3% isoflurane anesthesia and the osteochondral explants were harvested. All the samples were fixed in 4 % formalin for 1 week for further processing. This animal experiment complied with the ARRIVE guidelines and was approved by the Ethics Committee for Laboratory Animal Use (AVD101002016991; protocol #EMC 16-691-05).

2.6. *In vivo translational large animal osteochondral defect model*

A validated preclinical large animal bilateral osteochondral defect model was used to assess the osteogenic effect of the developed Sr-ACP

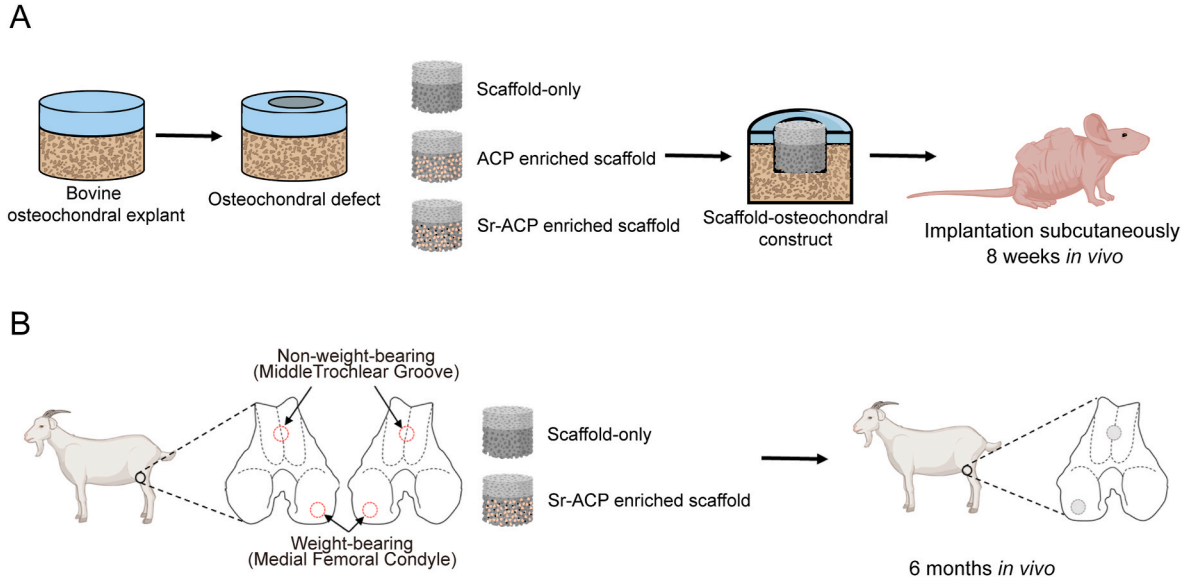

Fig. 2. Schematic experiment setup of *in vivo* models. (A) *In vivo* osteochondral defect model in the mouse. (C) *In vivo* osteochondral defect model in the goat.

enriched Col/Col-Mg-HAp scaffold. A gender balanced (6 castrated male goats and 6 female goats) experimental unit of 12 skeletally mature Saanen goats (age: 2–3 years, weight: 35.8 ± 6.6 kg) was subjected to a bilateral arthrotomy under general anesthesia as described before [42–44]. In short: all animals received a prophylactic antibiotic injection with amoxycillin clavulanic acid 8.75 mg/kg intramuscular (Noroclav, Norbrook, Ireland) and were intravenously sedated with butorphanol (0.2 mg/kg, Butador, Chanelle Pharma, Ireland) and diazepam (0.2 mg/kg, Diazemuls; Accord Healthcare, UK). A lumbosacral epidural block with lidocaine (2 mg/kg, Lidocaine HCl 2 %, B. Braun Medical Inc., EU, Melsungen, Germany) and morphine (0.2 mg/kg, Morphine Sulphate 10 mg/mL, Kalceks, Latvia) was performed with the animal in sternal recumbency. Anesthesia was induced with propofol IV to effect (max. 6 mg/kg, Propofol-Lipuro 1 %, B. Braun Medical Inc., Melsungen, Germany) and was maintained with isoflurane (Vetflurane, Virbac Animal Health, Suffolk, UK) in 100 % oxygen via a circle rebreathing system. All animals received analgesia with meloxicam IV (0.5 mg/kg, Rheumocam, Chanelle, Galway, Ireland); and morphine IV (0.2 mg/kg, Morphine sulphate, Mercury Pharmaceuticals, Dublin, Ireland) 90 min after the epidural block.

An arthrotomy of each stifle joint was performed in dorsal recumbency using a lateral parapatellar approach. Under constant irrigation with saline, a pointed 6 mm drill bit was used to drill an approximate 3–4 mm deep non-weight-bearing defect in the transition of the distal 1/3 to the middle 1/3 of the trochlear groove and in the central weight-bearing part of the medial femoral condyle. Subsequently, a custom-made flattened drill bit and a depth guide were used to create an exact flat 6 mm deep by 6 mm wide circular critical-sized osteochondral defect in the non-weight-bearing and weight-bearing location. The joint was flushed with saline to remove any debris, and the defects were press fit with a similar-sized selected scaffold before surgical closure as described before. The left and right stifle joints of each goat were randomly assigned to one of the two treatment groups (within animal controlled) (Fig. 2B): 1) Col/Col-Mg-HAp scaffold-only, and 2) Sr-ACP enriched Col/Col-Mg-HAp scaffold.

Following surgery, postoperative analgesia was provided (meloxicam 5 days) and goats were housed in indoor pens for daily postoperative welfare monitoring and scoring. Two weeks postoperatively, following the removal of skin sutures, animals were released to pasture or loose housing (weather dependent) for the remainder of the study period with daily health checks. An orthopaedic assessment (Table S1) was performed on the day of humane euthanasia under sedation with a barbiturate overdose at the predetermined endpoint at 6 months after surgery. Subsequently, all the joints, surrounding joint tissues, and synovial fluids were scored (Table S2), dissected, and photographed (Body Canon EOS R5, lens: Canon EF 100 mm f/2.8 L Macro IS USM, flash: Macro Ring lite MR-14EX II). Biopsies 1 cm by 1 cm square containing the entire osteochondral defects were harvested with an oscillating saw.

This animal experiment complied with the ARRIVE guidelines. Ethical evaluation and approval were provided by the Health Products Regulatory Authority of Ireland (AE1898217/P142), the Animal Research Ethics Committee of University College Dublin (AREC-18–17-Brama) and the Lyons Animal Welfare Board (Health, Husbandry and Monitoring plans; 201,907).

2.7. Macroscopic assessment of osteochondral defect repair

The quality of defect repair was assessed semi-quantitatively using the International Cartilage Repair Society (ICRS) macroscopic evaluation system (Table S3) [45] and a macroscopic scoring system (Table S4) developed by Goebel et al. [46]. The ICRS scoring system rates cartilage repair tissue as Grade IV (severely abnormal), Grade III (abnormal), Grade II (nearly normal) or Grade I (normal). The Goebel Score describes articular cartilage repair with five major evaluation categories. The quality of defect repair was scored blinded on fresh samples by two independent assessors, and the scores were averaged for further calculation. All the samples were fixed in 4 % formalin for 10 days after the macroscopic assessment.

2.8. Micro-computed tomography of subchondral bone defect repair

The harvested samples underwent micro-CT scans (Quantum GX2, Perkin Elmer, USA) after fixation in 4 % formalin *ex vivo*. For the bovine explants from the mouse model, the settings were: energy 90 KV, intensity 88 μA, 18 mm FOV, 36 μm isotropic voxel size. The micro-CT scan settings for goat samples were: energy 90 KV, intensity 88 μA, 36 mm FOV, 72 μm isotropic voxel size. All the scans were under an x-ray filter of Cu (thickness = 0.06 mm) and Al (thickness = 0.5 mm), and were calibrated using phantoms with a known density of 0.75 g/cm^3, which were additionally scanned before and after each scan. A high-resolution mode was set, and a scan time of 4 min was used. Image processing included modest Gauss filtering (sigma = 0.8 voxel, width = 1 voxel) and segmentation using a single threshold. A cylindrical region (4 mm diameter and 5 mm height) in the defect was selected as a volume of interest (VOI). In this VOI the following morphometric parameters were measured: bone volume per total volume (BV/TV), trabecular thickness (Tb·Th), trabecular number (Tb·N), and trabecular separation (TB.Sp). Morphological analyses were performed using IPL (Scanco Medical AG, Wangen-Brüttisellen, Switzerland).

2.9. Histology of osteochondral defect repair

After micro-CT scanning, the bovine osteochondral explants from the mouse model were decalcified using 10 % ethylenediaminetetraacetic acid (EDTA) for 4 weeks. The goat samples were decalcified for 3 weeks using 10 % formic acid. Subsequently, all samples were embedded in paraffin and sectioned in 6 μm thin sections. To study general cell and tissue morphology, H&E staining was performed with Hematoxylin (Sigma, Saint Louis, USA) and Eosin Y (Merck, Kenilworth, USA). Safranin-O staining was performed with 0.1 % Light green O (Fluka, Buchs, Switzerland) and 0.1 % Safranin-O (Fluka, Buchs, Switzerland) to visualize glycosaminoglycans in the extracellular matrix (ECM). To demonstrate the osteoclasts in the defects, Tartrate-resistant acid phosphatase (TRAP) staining was performed. Briefly, dewaxed sections were pre-incubated in sodium acetate (Sigma, Saint Louis, USA) and L (+) tartaric acid (Acros Organics, NJ, USA) buffer at room temperature for 20 min. Then naphthol AS-BI phosphate (Sigma, Saint Louis, USA) and fast red TR salt (Sigma, Saint Louis, USA) were added to the buffer and the slides were further incubated for 3 h at 37 °C. To discriminate between calcified and non-calcified osteochondral tissue, RGB staining was performed using Alcian Blue (Sigma, Saint Louis, USA), Fast Green (Sigma, Saint Louis, USA), and Picrosirius Red (Sigma, Saint Louis, USA).

NDP Software View2 (version 2.8.24, 2020 Hamamatsu Photonics K·K.) was used to measure the tissue volume in the osteochondral defect at three sections that were taken at the centre of the defect, and 0.5 mm and 1 mm from the centre for bovine explants from the mouse model or at the centre of the defect for the goat samples (Supplementary Figure 1). The percentage of the defect covered with newly formed osteochondral tissue was calculated (Supplementary Figure 2). Tissue volume in goat samples was independently measured by two investigators blinded to the experimental condition. The measurements of the two investigators were averaged for each section.

2.10. Statistical analysis

All statistical tests were performed using SPSS software 28.0 (SPSS inc., Chicago, USA). Comparisons in cytotoxicity assessment were analysed by a Kruskal-Wallis test. Multiple comparisons between scaffold-only, ACP enriched scaffold and Sr-ACP enriched scaffold groups in bovine explants from the mouse model were analysed by a One-Way ANOVA test or a Kruskal-Wallis test (depending on normality tested

by a Shapiro-Wilk test). Statistically significant differences between the scaffold-only group and the Sr-ACP enriched scaffold group, or between trochlear groove and femoral condyle groups in goat samples were determined by a Paired T test or a Wilcoxon signed-rank test (depending on normality tested by a Shapiro-Wilk test). A p-value ≤ 0.05 was considered statistically significant.

3. Results

3.1. Characterization of ACP/Sr-ACP granules

The modified wet precipitation technology successfully yielded ACP and Sr-ACP materials. An overview of ACP/Sr-ACP granule physico-chemical characteristics are given in Table 1, Figs. 3 and 4. The XRD patterns confirmed the amorphous character of the obtained products (Fig. 3A). The experimental Sr concentration of Sr-ACP (Table 1) was determined with ICP-MS at 2.49 ± 0.04 wt% (n = 3), which compared well with the theoretical value of 2.5 wt%. SEM-EDS mapping of chemical elements demonstrated homogenous Sr distribution within the Sr-ACP granules (Fig. 4C and D). The FT-IR spectra demonstrated the hydrated and carbonated nature both of ACP and Sr-ACP (Fig. 3B). Introduction of Sr ions in the given concentration for the as-synthesized materials did not reveal any structural changes that could be observed with XRD and FT-IR. Additionally, XRD and FT-IR measurements were performed on the same materials 3.5 years after manufacturing to check stability of the amorphous phase (Fig. 3C and D). The obtained XRD patterns demonstrated that ACP has started to crystallize while Sr-ACP has remained amorphous. In the FT-IR spectra of ACP, phosphate band shifts from 1002 cm^{-1} to 1010 cm^{-1} and from 549 cm^{-1} to 554 cm^{-1} were detected in parallel with the appearance of a band shoulder at 594 cm^{-1} for the 3.5-year-old sample. The band shoulder at 594 cm^{-1} confirms crystallization of ACP to some extent as already demonstrated by the XRD data as splitting of phosphate bands around 1000 cm^{-1} and 550 cm^{-1} usually indicates crystallization of ACP materials [47]. The specific surface area of both ACP and Sr-ACP granules was high (>100 m^2/g) with particle size d_{BET} being 20–21 nm (Table 1). The dry granulation technology produced irregular shape granules with sharp edges (Fig. 4A and B). The sharp edges of the granules originate from the milling of the ACP agglomerates. Granule surfaces at the macro level were smooth and non-porous. By measuring granule dimensions from the SEM images, an average value of the experimental granule size was determined to be 187 ± 35 μm (at least 100 granules were measured for each sample).

The final step of the granule production was granule washing with ethanol to remove any debris that may have originated from the granulation process. To assess whether the rinsing procedure has an impact on the structure of the ACP materials, granules were characterized with FT-IR (Supplementary Figure 3). No differences in FT-IR spectra of ACP granules before and after the rinsing with ethanol were detected.

Before *in vitro* and *in vivo* experiments, materials must be sterilized; in this study, gamma irradiation was used. To ensure amorphous granule composition remained unaffected post-sterilization, phase and chemical composition were analysed using XRD and FT-IR. Obtained results demonstrated that gamma irradiation sterilization of ACP granules was effective, with no detectable changes in composition or crystallinity (Supplementary Figure 4).

Table 1
Values of Sr concentration, specific surface area (SSA), and calculated particle size d_{BET} for ACP and Sr-ACP granules.

	Sr conc., wt%	SSA, m^2/g	d_{BET}, nm
ACP	0.01	113 ± 2	21
Sr-ACP	2.49 ± 0.04	115 ± 2	20

3.2. ACP/Sr-ACP granule containing Col/Col-Mg-HAp scaffolds

The addition of ACP/Sr-ACP granules to the Col/Col-Mg-HAp scaffold is an additional step for the manufacturing process of the scaffolds. The newly developed ACP/Sr-ACP granule containing Col/Col-Mg-HAp scaffolds were examined with two-dimensional SEM and three-dimensional micro-CT analyses to assess granule 3D distribution within the ACP granule containing scaffolds. The Sr-ACP granules were well and homogeneously distributed in the bottom layer of scaffold (Fig. 5A). The SEM image (Fig. 5B) shows the bilayered structure of the scaffold as well: collagen-only layer on top and Col-Mg-HAp-Sr-ACP layer on the bottom. Both layers of the freeze-dried scaffold have a porous structure, which is governed by collagen. In the bottom layer the incorporated micron-sized Sr-ACP granules can be seen, while the nanoparticles of Mg-HAp cannot be visualized at given magnification. The shown SEM-EDS element maps of Ca, P, Sr, C, and Mg of Sr-ACP enriched Col/Col-Mg-HAp scaffolds (Fig. 5C) and ACP enriched Col/Col-Mg-HAp (supplementary Figure 5) demonstrate localization of the chemical elements within the scaffolds. EDS element maps of the same area (Fig. 4C) confirm the presence of the Sr-ACP granules as well. As Ca and P are the main constituents of Sr-ACP, the high contrast areas in Ca and P element maps match Sr-ACP granule placement in the SEM image (Fig. 5B). The presence of Sr is detected as well. The EDS map of Mg designates the location of the biomimetically deposited Mg-HAp nanoparticles onto the fibers of the collagen scaffold's bottom layer (Fig. 5C). The EDS map of C demonstrates the presence of collagen throughout the mapped area; higher intensity area of C is visible for the top layer which contains only collagen and no calcium phosphates (Fig. 5C). SEM inspection of Sr-ACP granule containing scaffolds showed that the granules have a good compatibility with the scaffold's main component - collagen. SEM images (Fig. 5D), showed that the ACP granules were incorporated in the collagen fibers of the scaffold. Collagen fibers were attached to the surface of the granules and stretched across it.

3.3. Cytotoxicity assessment

The *in vitro* cell viability was assessed to evaluate the possible cytotoxicity of the developed ACP/Sr-ACP granules. The 25 %, 15 %, 8 % and 2.5 % dilutions of extracts that were harvested after 24-h incubation of ACP or Sr-ACP (2.49 wt% Sr) granules were not cytotoxic (Fig. 6A). To assess the biocompatibility of ACP or Sr-ACP enriched Col/Col-Mg-HAp scaffolds, scaffolds with 30 wt% ACP or Sr-ACP granules were prepared for cytotoxicity assessment. 100 % extracts from all the scaffolds were cytotoxic, and ACP or Sr-ACP enriched Col/Col-Mg-HAp scaffolds reached a non-cytotoxic level from dilution 16 % (Fig. 6B).

3.4. Effect of ACP and Sr-ACP addition to the scaffold on osteochondral defect repair in an in vivo mouse subcutaneous model

An *in vivo* early osteochondral repair phase semi-orthotopic mouse model was used to assess the *in vivo* compatibility and osteogenic effect of ACP or Sr-ACP enriched Col/Col-Mg-Hap scaffolds. After 8 weeks, remnants of the collagen-only layer were observed in the cartilage region of the defect, while the Col-Mg-HAp layer in the subchondral bone defect was mostly degraded and replaced by bone-like tissue (Fig. 7A). Notably, ACP or Sr-ACP granules can still be seen after 8 weeks, and were well distributed in the newly formed tissues (Fig. 7A). Some osteoclasts attaching to the granules in the bone tissue were demonstrated by TRAP staining (Fig. 7A). The subchondral bone defects were filled with newly formed osteochondral tissue, indicating good biocompatibility and osteogenic property of ACP and Sr-ACP granules. Slightly more osteochondral repair tissue was found in the osteochondral defects loaded with Sr-ACP enriched scaffolds (89.3 ± 7.2 %) compared to the scaffold-only (87.2 ± 11.1 %) or ACP enriched scaffolds (80.2 ± 21.5 %), although no significant differences in tissue volumes were found (Fig. 7B).

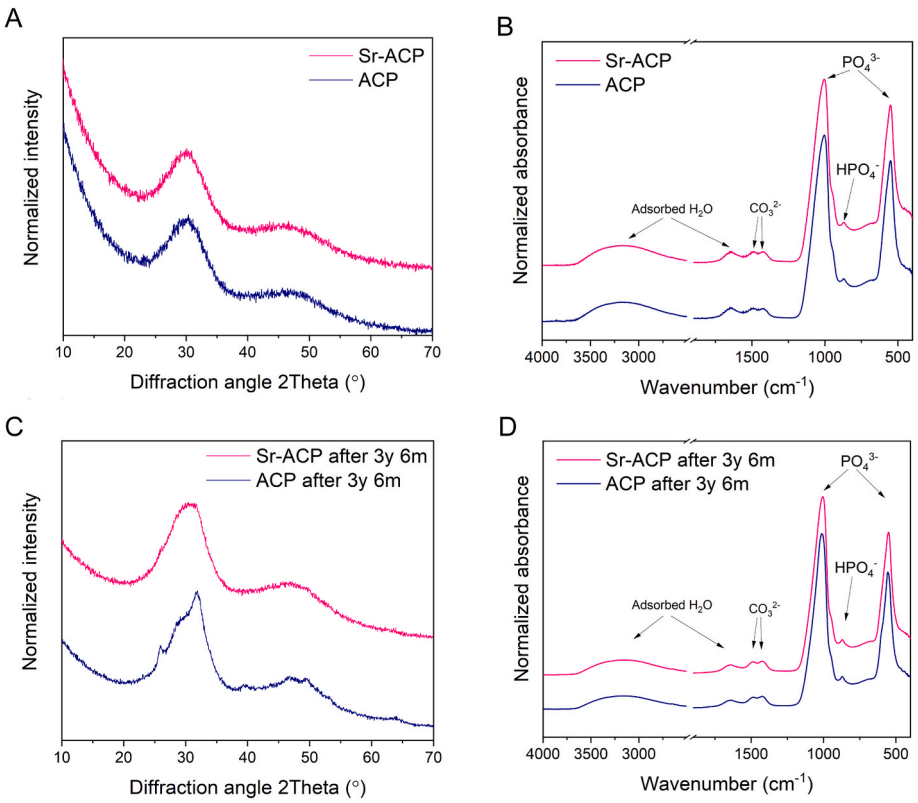

Fig. 3. Phase and chemical group composition of ACP and Sr-ACP. (A) XRD patterns showing wide diffraction maxima indicative of the amorphous phase of the as-synthesized ACP and Sr-ACP, (B) FT-IR spectra demonstrating chemical group information, hydrated and amorphous nature of ACP and Sr-ACP, (C) XRD patterns and (D) FT-IR spectra of ACP and Sr-ACP after 3.5 years of storage in air at room temperature (20 ± 2 °C) in a sealed container.

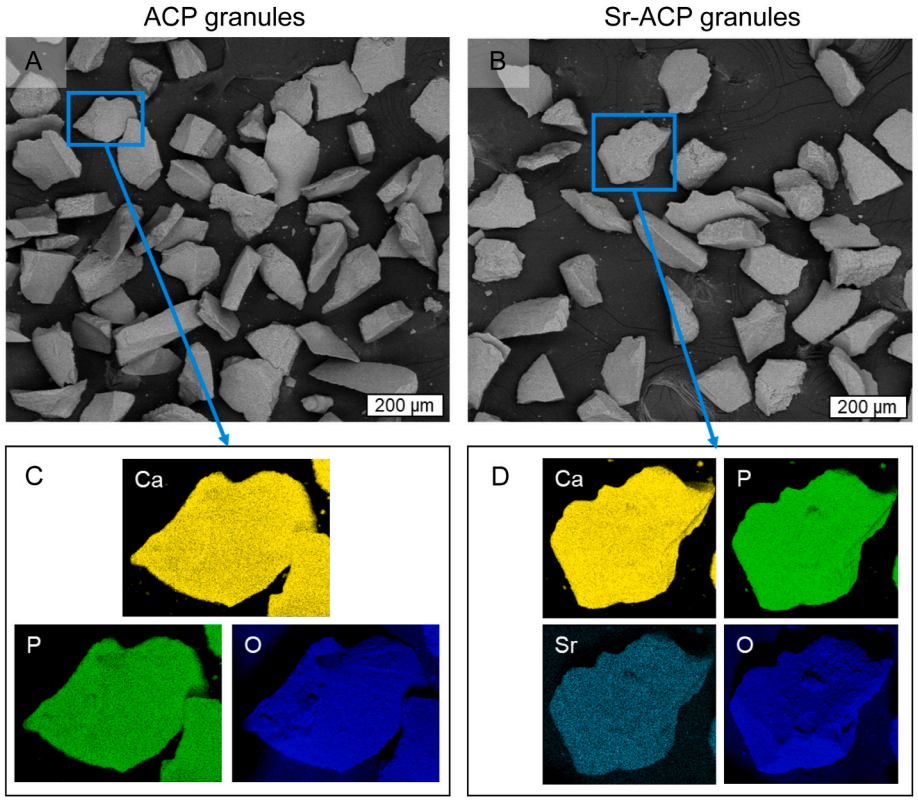

Fig. 4. Morphology and chemical element distribution of ACP and Sr-ACP granules. SEM images of ACP (A) and Sr-ACP (B) irregularly shaped granules. SEM-EDS element maps of selected ACP (C) and Sr-ACP (D) granules demonstrate homogenous chemical composition, where each material's main elements are shown.

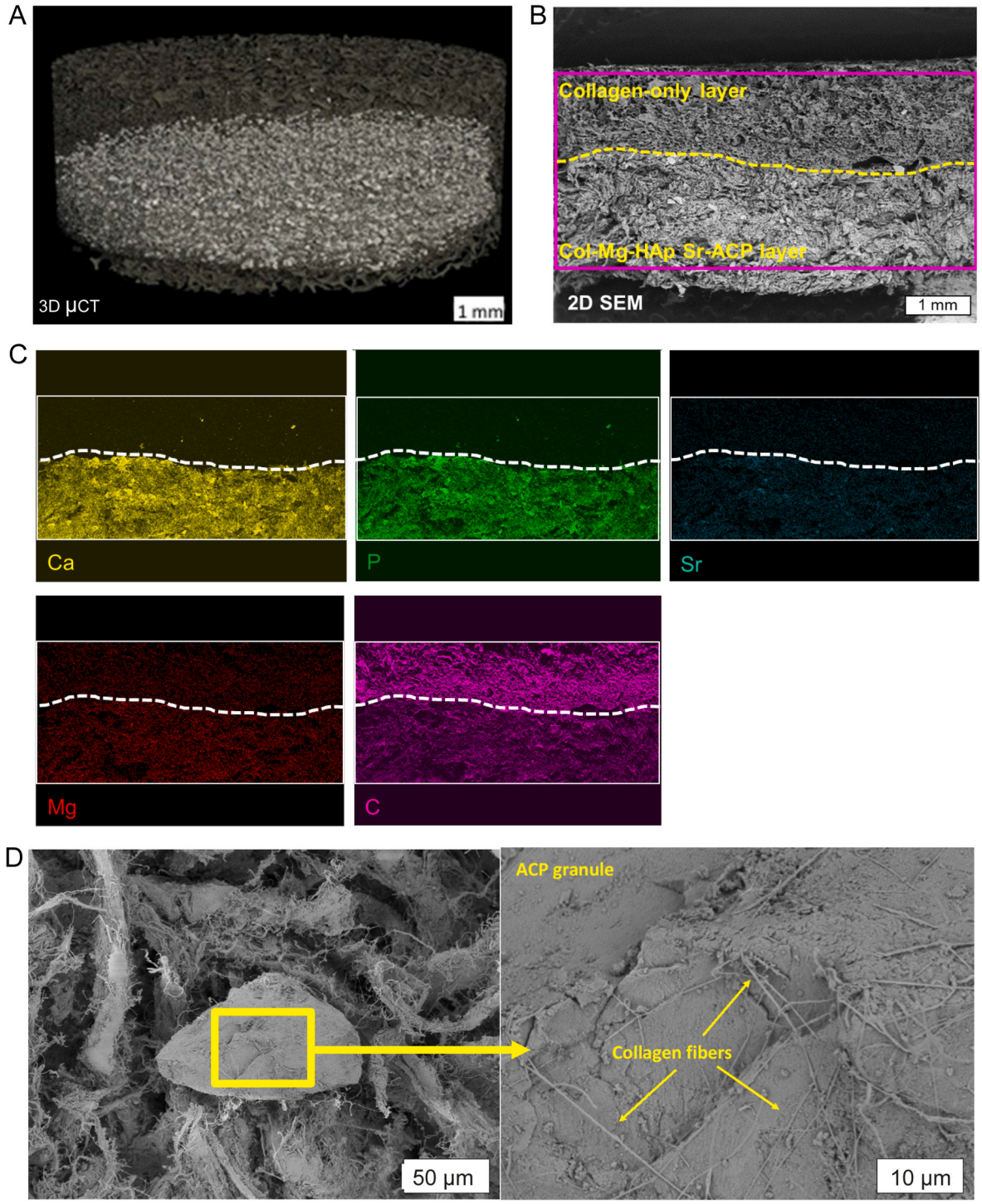

Fig. 5. Characterization of Sr-ACP enriched Col/Col-Mg-HAp scaffold. Representative three-dimensional micro-CT image (A) of Sr-ACP granule containing Col/Col-Mg-HAp scaffold. SEM image in backscattered electron (BSE) detector mode (B) of cross-section of the Sr-ACP granule containing Col/Col-Mg-HAp scaffold, where the top layer is collagen and the bottom layer is Col-Mg-HAp layer enriched with Sr-ACP granules, and where the drawn rectangle marks EDS mapping area. EDS element (Calcium, Ca - yellow, Phosphorus, P - green, Strontium, Sr – light blue, Magnesium, Mg - red, Carbon, C - magenta) maps (C) of the scaffold visualized on (B), where the dashed line shows the border between both layers and the brightest areas in Ca and P maps represent positions of the Sr-ACP granules SEM images of Sr-ACP granule containing scaffold (D) where single ACP granule (left) and close-up view of the surface of the Sr-ACP granule covered in collagen fibers (right) is shown.

3.5. Effect of Sr-ACP on osteochondral defect repair in an in vivo large animal translational model

3.5.1. Clinical observations and scaffold implantation

The Sr-ACP enriched Col/Col-Mg-HAp scaffold demonstrated good repair in the mouse model and therefore the osteogenic capacity of Sr-ACP granules was further investigated in a validated translational goat osteochondral defect model in the knee. Scaffolds were successfully implanted into osteochondral defects created in the trochlear groove (a non-weight-bearing location) and the medial femoral condyle (a weight-

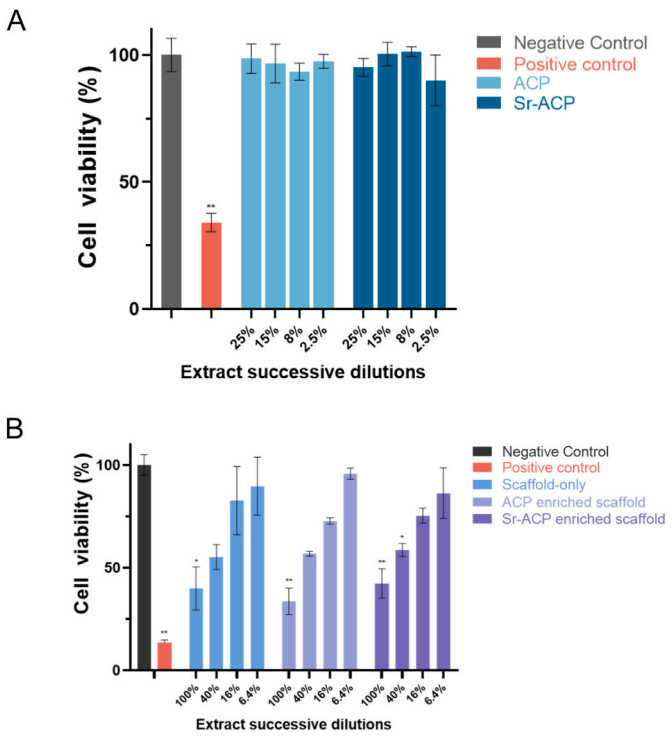

Fig. 6. Cytotoxicity of the developed ACP/Sr-ACP granules and scaffolds. Cytocompatibility evaluation of Balb/c 3T3 clone A31 cells exposed to ACP/Sr-ACP granules extraction (A, n = 4) and ACP/Sr-ACP enriched scaffold extraction (B, n = 3). Cell viability (%) is the ratio of test condition and negative control. Negative control is complete culture medium only. Phenol was added in the positive control. **P < 0.01, *P < 0.05 compared to negative control.

bearing location) of both knees. All animals recovered well post-operatively except for one goat that died 2 weeks post-surgery due to clostridium disease unrelated to the surgery or the experiment. The macroscopic appearance 2 weeks post-surgery showed that scaffolds were stable at both medial femoral condyle and trochlear groove osteochondral defect sites (Supplementary Figure 6A). The two layers of the scaffold can clearly be seen in the osteochondral defects histologically at two weeks (Supplementary Figure 6B). Another two goats died at 4- and 5-months post-surgery, again caused by clostridium disease despite vaccination and unrelated to the surgery and the experiment. The remaining eight goats were in good health throughout the study. At the predetermined 6-month endpoint the orthopedic exam demonstrated normal locomotion and excellent joint mobility in all goats.

All the joints, surrounding joint tissues, and synovial fluid were scored macroscopically on opening of the joints. There was no evidence of inflammatory responses or construct delamination in the treated joints at the time of retrieval. No joint swelling, effusion, mobility abnormalities or adhesions were found. Synovial fluid and membrane were normal and no indications of patellar instability/luxation were found.

3.5.2. *Tissue repair in the osteochondral defects*

The samples from the goats that unexpectedly died at 4 and 5 months post scaffold implantation revealed that the scaffolds had been degraded completely, and the osteochondral defects were mostly filled with repair tissue demonstrated by H&E, Safranin-O and RGB staining (Supplementary Figure 7). Overall, at 6 months, well-structured subchondral trabecular bone was observed in most trochlear groove and femoral condyle subchondral bone defects demonstrated by reconstructed micro-CT images, macroscopic sectional view and histology (Figs. 8 and 9, Supplementary Figure 8). Reconstructed subchondral bone defect images showed an area with no trabecular bone either underneath or at the bottom of the defects unrelated to the defect location or the scaffold type. Histological images demonstrated that these areas found in micro-CT images were filled with bone marrow and were dissimilar to cysts.

In the non-weight-bearing trochlear groove location reconstructed micro-CT images showed no significant difference in the BV/TV, Tb. Th, Tb. N and Tb. Sp within animals between subchondral bone defects filled with scaffold only or Sr-ACP enhanced scaffolds (Fig. 8A and B). The macroscopic cross-sectional view and histology further confirmed the well-repaired subchondral bone (Fig. 9C). Bone-like tissue (including the bone marrow) was quantified on RGB stained histology. After 6 months, slightly more bone tissue (98.0 ± 29.0 % vs. 92.7 ± 11.9 %, P = 0.499) was found in the subchondral bone defects when the Sr-ACP was incorporated into the scaffolds compared to the scaffold-only, although no statistically significant difference was found (Fig. 9D).

In the weight-bearing femoral condyle location no significant difference in the BV/TV, Tb. Th, Tb. N, and Tb. Sp was observed at 6 months within animals between subchondral bone defects filled with scaffold only or Sr-ACP enhanced scaffolds (Fig. 9A and B). Overall, 96.9 ± 3.8 % (scaffold-only group) and 96.0 ± 5.6 % (Sr-ACP enriched scaffold) of the subchondral bone defects were filled with osteochondral tissue (Fig. 8C and D). However, when looking specifically at the study target, the bone layer of the osteochondral unit, significantly more bone tissue was found (P = 0.029, Fig. 8D) in the subchondral defects loaded

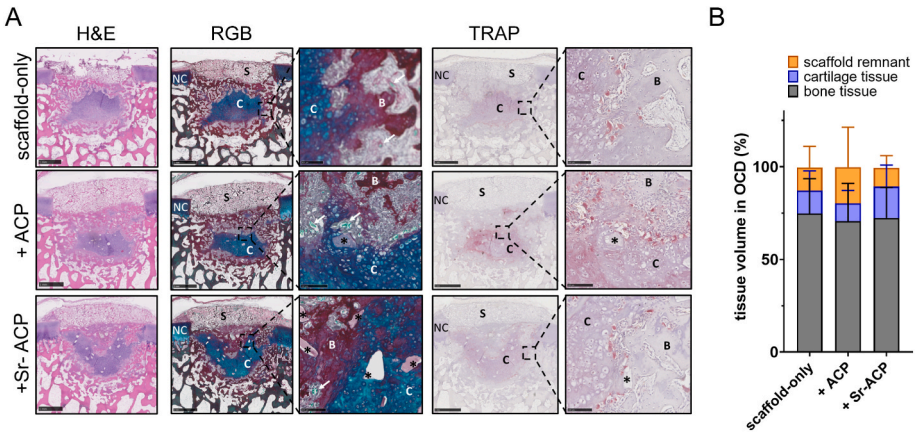

Fig. 7. ACP and Sr-ACP showed a good biocompatibility for osteochondral repair *in vivo*. (A) Representative images of the 8-week repair constructs stained with H&E (Hematoxylin and Eosin), RGB (Alcian Blue, Fast Green, and Picrosirius Red) and Tartrate-resistant acid phosphatase (TRAP) staining. Scale bars indicate 1 mm and 100 μm, respectively. NC: native cartilage; C: newly formed cartilage-like tissue; B: newly formed bone-like tissue; S: remnants of the scaffolds; *: ACP or Sr-ACP granules. (B) The percentage of tissue volume calculated in the osteochondral defects (OCD). The repair tissue volume was expressed as mean ± standard deviation (SD). No significant difference was found among the three conditions.

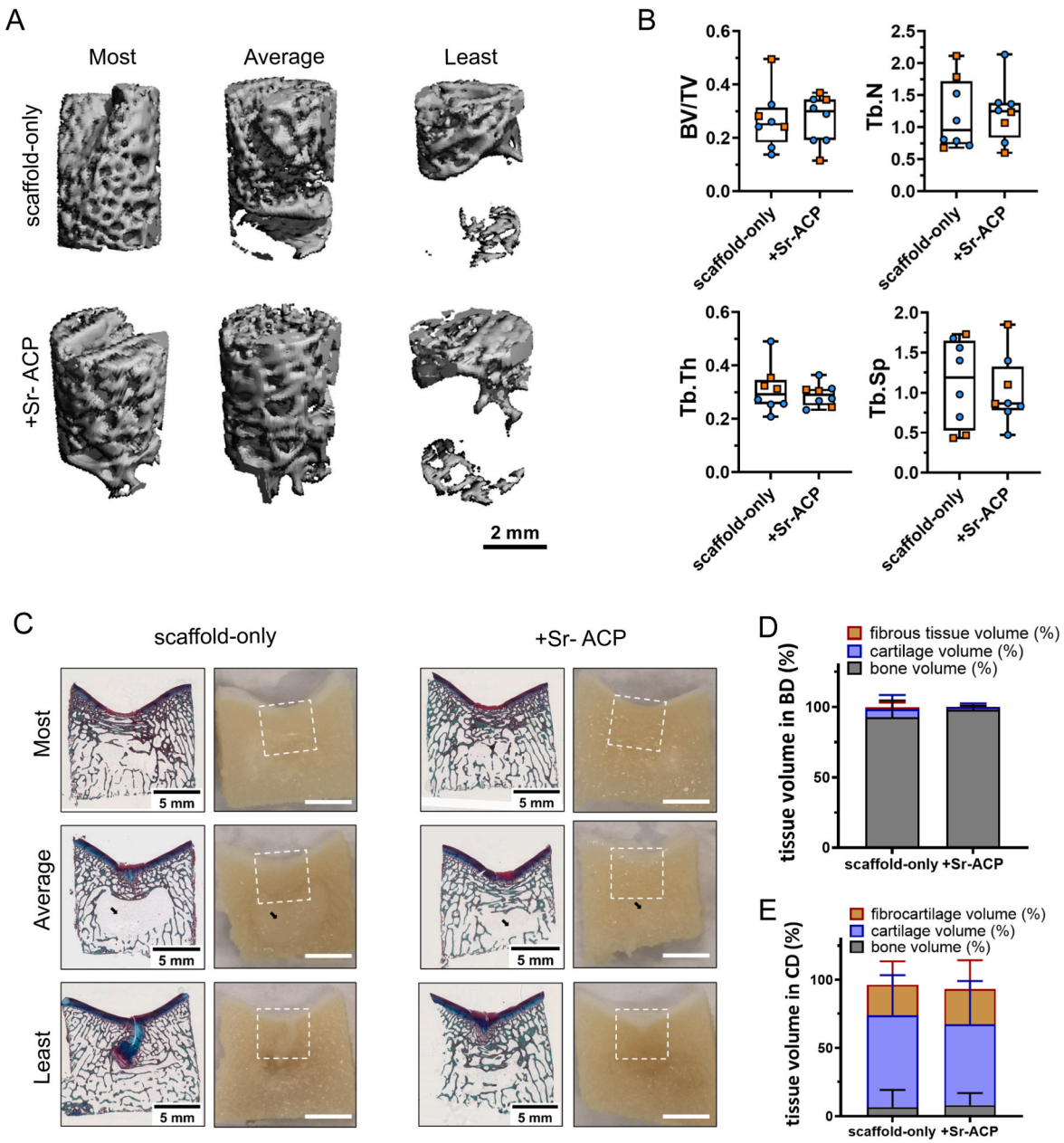

Fig. 8. Tissue repair in the trochlear groove defect sites. (A) Representative micro-CT reconstructions treated with either scaffold-only or Sr-ACP enriched scaffold. Samples with most, average, and least bone volume are presented. The scale bar indicated 2 mm. (B) BV/TV, trabecular thickness (Tb. Th [mm]), trabecular number (Tb. N [1/mm]), and trabecular separation (Tb. Sp [mm]) in the bone defects after 6 months. Blue circles indicate castrated male goats, orange squares indicate female goats. The box plots indicate the minimum, first quartile, median, third quartile, and maximum. No significant difference was found between the two conditions. (C) RGB (Alcian Blue, Fast Green, and Picrosirius Red) staining and macroscopically sectional view of osteochondral defects treated with either scaffold-only or Sr-ACP enriched scaffold. H&E staining and Safranin-O staining of the same samples are presented in Supplementary Fig. 8. Samples with most, average, and least bone-like tissue in bone defects are presented. White squares indicated 6*6 mm osteochondral defects. Black arrows indicated the structure with only bone marrow. The scale bar indicates 5 mm. (D) The percentage of tissue volume calculated in the subchondral bone defects (BD). The repair tissue volume was expressed as mean ± standard deviation (SD). (E) The percentage of tissue volume calculated in the cartilage defects (CD). The repair tissue volume was expressed as mean ± standard deviation (SD). No significant difference in tissue volume in both cartilage defects and bone defects was found between the two conditions.

with Sr-ACP enriched scaffold (88.6 + 7.6 %) compared to scaffold-only (76.7 ± 11.4 %).

Interestingly, more bone-like tissue was regenerated in the trochlear groove subchondral bone defect sites compared to the medial femoral condyle subchondral bone defect sites when scaffold-only (92.7 ± 11.9 % vs. 76.7 ± 11.4 %, P = 0.062) or Sr-ACP enriched scaffolds (bone-like tissue: 98.0 ± 2.9 % vs. 88.6 ± 7.6 %, P = 0.025) were implanted in the osteochondral defects.

The cartilage part of the defects treated with either scaffold was repaired well with good integration into the surrounding native tissue macroscopically at 6 months post-implantation (Supplementary Figure 9). Only small, scattered fissures or cracks were observed on some surfaces of the defects and no noticeable depressions were observed overall. In trochlear groove defects (Supplementary Figure 9A), the macroscopic ICRS and Goebel scores for the scaffold-only group had a median score of 10.19 ± 1.65 out of 12 and 17.19 ± 3.39 out of 20, respectively (Supplementary Figure 9B). All the samples were classified as normal (grade I) or nearly normal (grade II) cartilage except for one

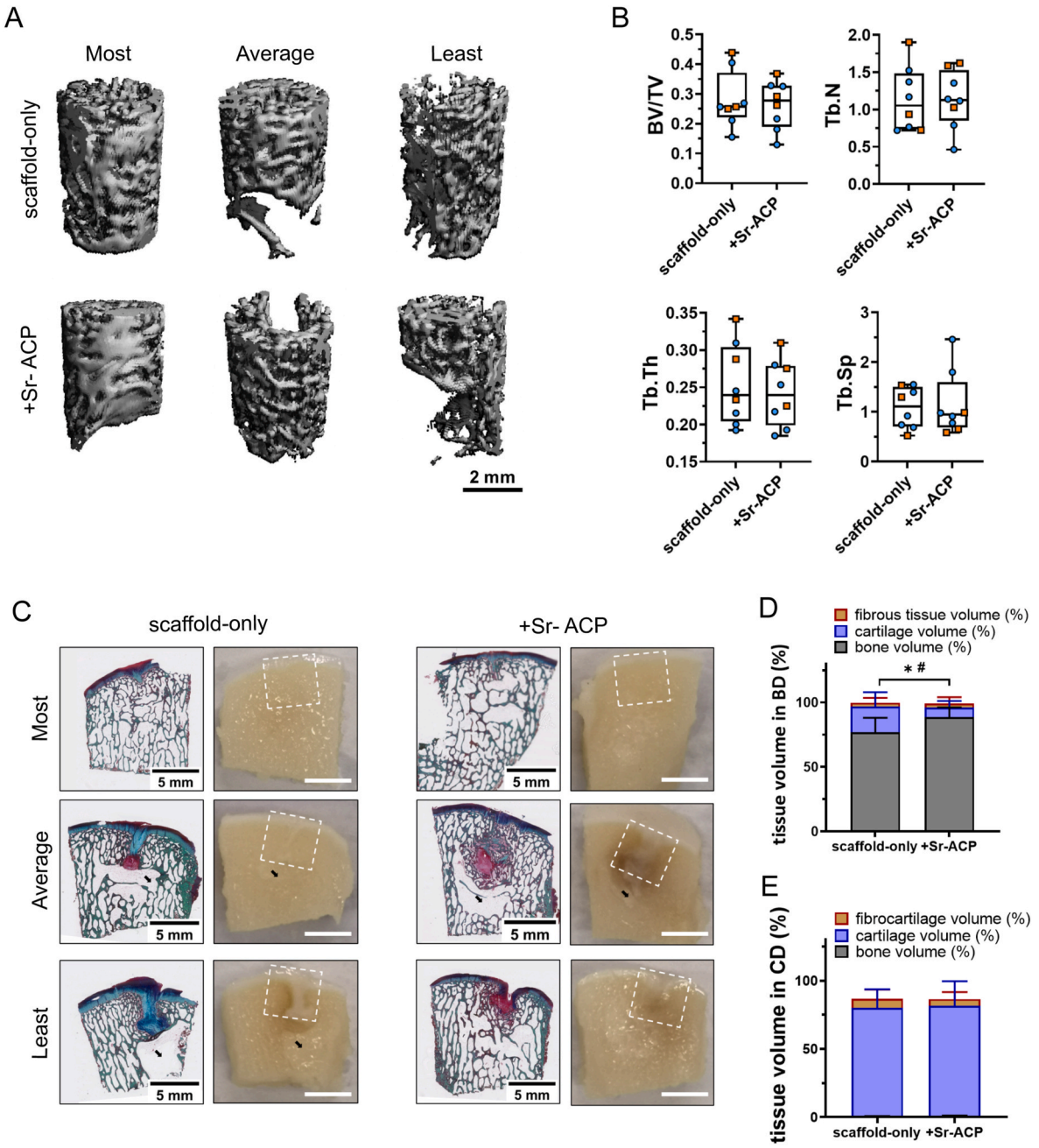

Fig. 9. Tissue repair in the femoral condyle defect sites. (A) Representative micro-CT reconstructions treated with either scaffold-only or Sr-ACP enriched scaffold. Samples with most, average, and least bone volume are presented. The scale bar indicates 2 mm. (B) BV/TV, trabecular thickness (Tb. Th [mm]), trabecular number (Tb. N [1/mm]), and trabecular separation (Tb. Sp [mm]) in the subchondral bone defects after 6 months. Blue circles indicate castrated male goats, orange squares indicate female goats. The box plots indicate the minimum, first quartile, median, third quartile, and maximum. No significant difference was found between the two conditions. (C) RGB (Alcian Blue, Fast Green, and Picrosirius Red) staining and macroscopic images of osteochondral defects treated with either scaffold-only or Sr-ACP enriched scaffold. H&E staining and Safranin-O staining of the same samples are presented in Supplementary Fig. 8. Samples with most, average, and least bone-like tissue in bone defects are presented. White squares indicated 6*6 mm osteochondral defects. Black arrows indicated the structure with only bone marrow. The scale bar indicated 5 mm. (D) The percentage of tissue volume calculated in the subchondral bone defects (BD). The repair tissue volume was expressed as mean ± standard deviation (SD). *P < 0.05 in cartilage-like tissue, #P < 0.05 in bone-like tissue. (E) The percentage of tissue volume calculated in the cartilage defects (CD). The repair tissue volume was expressed as mean ± standard deviation (SD). No significant difference in tissue volume in cartilage defects was found between the two conditions.

sample (grade III). For the Sr-ACP enriched scaffold group, the macroscopic ICRS and Goebel scores were 9.50 ± 2.98 and 16.63 ± 3.93, respectively (Supplementary Figure 9B). Two defects repaired with the Sr-ACP enriched scaffold were classified as abnormal (grade III). Macroscopic assessment of femoral condyle defects repaired (Supplementary Figure 9C) with the scaffold-only resulted in median ICRS scores of 10.13 ± 0.83, and median Goebel scores of 18.69 ± 0.37 at 6 months (Supplementary Figure 9D). The defects fitted with the Sr-ACP enriched scaffold were scored median ICRS scores of 9.94 ± 1.27, and median Goebel scores of 18.56 ± 1.02 (Supplementary Figure 9D). All the samples were classified as nearly normal (grade II) cartilage. Overall, no significant difference was observed in cartilage repair between these two conditions with both scoring systems. Histologically, cells with a rounded morphology within the cartilage region were found residing

within lacunae and with alignment typical of native cartilage. Both scaffolds demonstrated cartilaginous tissue formation by positive GAG staining on RGB (Fig. 8C and 9C) and Safranin-O (Supplementary Figure 8) but no significant differences could be found between the scaffolds (Fig. 8E and 9E).

4. Discussion

The main finding of this study is that the addition of Sr-ACP granules into a clinically used osteochondral scaffold is a feasible and effective strategy to improve its bone repair capacity in *in vivo* osteochondral defects. The subcutaneous mouse osteochondral defect model demonstrated good biocompatibility and an overall good early tissue response of both ACP and Sr-ACP enriched Col/Col-Mg-HAp scaffolds, whereas a better bone formation was obtained in subchondral bone defects treated with the Sr-ACP enriched scaffolds in a weight-bearing subchondral bone defect at 6 months in a translational goat model.

The new strategy proposed in this study is based on the modification of a clinically used Col/Col-Mg-HAp scaffold through the incorporation of ACP or Sr-ACP granules with a high specific surface area (>100 m^2/g) and a hydrated and carbonated nature. A simple, fast, cost-effective, and scalable method for the preparation of ACP was used in this study and further modified for the preparation of Sr-ACP. Further, the manufactured ACP or Sr-ACP granules with a large specific surface area and hydrated and carbonated nature were well distributed in the Col/Col-Mg-HAp scaffold. Due to the potent effects of calcium and phosphate ions on bone cells, and their presence in large quantities in bone tissue, calcium phosphates (CaPs) are of high interest in the bone repair biomaterial field [48]. ACP is involved in the early stages of bone mineralization [49] and the formation of complex CaP structures during bone mineral shaping and structuring [48,50]. Previous studies on ACP have demonstrated excellent biocompatibility and bioactivity of this product *in vitro* [51] as well as good biodegradability, osteoconductivity, and osteogenic potential also in *in vivo* osteochondral defect models [52,53]. On the other hand, the main inorganic component of bone is low crystalline apatite that highly resembles the chemical structure of HAp [54–56]. The addition of HAp into the bone layer can further improve the osteogenic potential of a collagen-based scaffold *in vivo* [57–61]. Therefore, the combination of ACP and HAp materials in a biphasic manner was expected to improve bone regeneration in osteochondral defects. The high crystallinity and stoichiometry of HAp contribute to rather slow rates of dissolution, thereby improving mechanical properties of the scaffold and long-term bone regeneration [62]. ACP, in the meantime, can favour the onset of bone deposition in the early stages of remodelling with its high solubility and amorphous structure [50].

In addition, we have successfully combined an alternative local Sr^{2+} delivery carrier in the form of ACP granules within the Col/Col-Mg-HAp scaffold to further improve bone regeneration. Sr and Ca are chemically very similar in ion size and have the same charge (+2) [63], thus Sr incorporation in calcium rich materials can be achieved. The majority of *in vitro* studies support a dual effect of Sr^{2+} on bone tissue: 1) stimulating bone formation by increasing proliferation and differentiation of osteoblasts, and inhibiting their apoptosis [24,64–66]; 2) hindering bone resorption by inhibiting the formation and differentiation of osteoclasts and promoting their apoptosis [65–67]. Our *in vivo* mouse study showed good osteochondral defect repair with ACP or Sr-ACP enriched scaffolds after 8 weeks with osteoclasts attaching to the granules.

The possible structural transformation of ACP into other calcium phosphate compounds raised problems for mass production, processing and storage [50]. The synthesis route for the preparation of amorphous calcium phosphates we used in this study enabled stability of ACP in air in a dried state for at least 7 months [34]. Trace amounts of various ions have been corroborated to affect ACP transformation [68,69]. Mg^{2+} is an effective inhibitor for the ACP phase transformation by changing the internal structure of ACP and reducing solubility [70–72]. Furthermore, Sr^{2+} can stabilize ACP as well [68]. Interestingly, the presence of Sr^{2+} was reported to significantly enhance the stabilization effect of Mg^{2+} on ACP due to a synergic effect, which might be due to that Sr^{2+} promotes the exclusion of Mg during HAp nucleation from ACP [69]. In the current study, prolonged investigation of ACP and Sr-ACP stability was performed. Sr-ACP with 2.5 wt% of Sr was found to have amorphous phase stability in a dry state of at least 3.5 years while ACP without Sr demonstrated signs of crystalline transformation. Therefore, a relatively stable phase of ACP was expected in a Col/Col-Mg-HAp-Sr-ACP scaffold before implantation. After implantation Sr-ACP/ACP granules eventually would transform into a poorly crystalline calcium phosphate phase resembling bone mineral. Our *in vivo* studies demonstrated that incorporated granules were still present after 8 weeks in mice, and were degraded after 4 months in goats, when there was already sufficient bone regeneration, although the composition (Sr-ACP/ACP granules or calcium phosphate phase) of the granules found on histology was not confirmed.

Here, the Col/Col-Mg-HAp scaffolds modified with ACP and Sr-ACP were investigated on the sequential use for osteochondral defects in *in vivo* models, from a small animal model to a translational large animal model. These two models, used together, allowed us to investigate the possible effect of incorporating ACP or Sr-ACP into the Col/Col-Mg-HAp scaffold used for osteochondral repair and to bring our approach a step closer to the physiological and mechanical conditions in the human osteochondral environment. Firstly, we confirmed biocompatibility and osteogenic properties of the modified Col/Col-Mg-HAp scaffolds in the mouse model as the first screening. The semi-orthotopic model allows a minimally invasive surgery and a multiple graft testing possibility [73], in line with the increasing ethical requirements on animal experiments. The results showed that, after 8 weeks, the bone-like layer in the subchondral bone defect was mostly degraded and replaced by bone-like tissue. The presence of repaired bone tissue together with the lack of side effects in all the experimental groups demonstrated a safe and good repair capacity of both ACP and Sr-ACP enriched scaffolds. In fact, both the native osteochondral Col/Col-Mg-HAp scaffold and the incorporated inorganic granules have been shown to be biocompatible and biodegradable [51–53,59,74,75]. The three treatment groups showed the presence of repair tissue. There is no significant difference among the different scaffolds. This indicates that the granule insertion did not interfere with the healing process. The scaffold-only condition also demonstrated excellent bone healing after 8 weeks in the mouse model. Smaller animals tend to heal quickly if compared with larger animals due to the intrinsic nature of osteochondral lesions [76]. Consequently, 8 weeks represents a relatively late time point in this model. Therefore, considering the quick repair response, and also the lack of synovial fluid, mechanical loading and complete immune system in the mouse [73], the use of a more advanced translational large animal model, suitable for comparison with human conditions, was a logical subsequent step. Thus, after the preliminary evaluation in mice, the most promising scaffold modification, the addition of Sr-ACP granules, was selected to be tested in a goat translational osteochondral defect model.

The goat model is a fully immune competent model using outbred animals, and offers advantages regarding joint size, cartilage and subchondral bone thickness, accessibility for surgical procedures, and limited intrinsic healing capacity [77]. Sex-balance was included in the experimental set up of this study as appropriate to enhance scientific rigor, but sadly unexpected and experimental unrelated animal deaths prevented a sufficiently powered analyses of sex differences. Therefore, no sex difference in subchondral bone repair was observed. The validated goat model provides the opportunity to assess tissue regeneration in paired knee joints within the same goat to reduce individual variation effects and enhance statistical power (within animal controls). The model also allows studying two different mechanical loading environments within the same joint. In particular, the Col/Col-Mg-HAp and the Sr-ACP enriched Col/Col-Mg-HAp scaffolds were successfully implanted in the trochlear groove, with no/low direct mechanical loading, and in the medial femoral condyle, with direct mainly compressional

mechanical loading [78]. In this goat model, significantly more bone was regenerated after 6 months in the subchondral bone defects of the biomechanically more challenging femoral condyle lesions when Sr-ACP was incorporated into the scaffold compared to scaffold-only. In fact, during its metabolism, bone incorporates and releases various trace elements (Na, Mg, Sr, Zn, Si etc.) into the cellular microenvironment [63]. Similar element/ion release in the cellular microenvironment was expected when Sr-ACP was incorporated into the Col/Col-Mg-HAp scaffold, where Sr^{2+}, Mg^{2+}, Ca^{2+}, and PO_4^{3-} should be released from the scaffold during the healing process, favouring chemotaxis, scaffold colonization, and the cell mineralization process, since this bone layer of the scaffold has a porous nano-structured composition aimed at the efficient delivery of ions [37].

In this study, our primary objective was to improve subchondral bone repair of osteochondral defects by incorporating newly developed Sr-ACP granules into the bone-like layer of the Col/Col-Mg-HAp scaffold. The cartilage-like layer of this scaffold has already been studied extensively and the excellent chondrogenic capacity of this Col/Col-Mg-HAp scaffold has been confirmed [79–81]. Briefly, the cartilage layer that consists of type I collagen-only demonstrated 3D support for the attachment and proliferation of human MSCs. Human MSCs seeded on the cartilage part of this scaffold changed toward chondrocytes, as evidenced by cell morphology and the formation of extracellular matrix demonstrated by the synthesis of type II Collagen (immunohistochemistry) and GAGs [79–81]. In the presented study, the cartilage part of the defects treated with either scaffold was repaired well with good integration into the surrounding native tissue, which is consistent with previous *in vitro*, preclinical and clinical results [12–14,79–81].

The overall good osteochondral regeneration obtained with the scaffold-only may have hindered the possibility to detect a significant improvement in this model, which did not show the same criticalities observed in terms of osteochondral regeneration in humans. In the more challenging and translational goat model, the incorporation of Sr-ACP into the scaffold was significantly more effective in regenerating bone tissue compared to the scaffold-only, as shown by the histological analysis. Overall, the scaffold-only and Sr-ACP enriched scaffolds regenerated a similar volume of osteochondral tissues, which means more cartilage-like tissue was present in the subchondral bone defect with the scaffold-only. These cartilage-like tissues might be ossified afterwards. In other words, there might be an acceleration effect of Sr-ACP at the earlier stage of repair. However, in this study, bone repair at only one time-point was assessed in the goat model. Therefore, the early cellular responsiveness that leads to a potential acceleration at this stage of repair, or long-term osteogenesis, which is known to end within 10–12 months [82], was not investigated. An effect could have been missed at its full extent by having a study focus of 6 months. This may also explain how, unlike what was observed by histological analysis, no significant difference in bone volume was found by micro-CT analysis.

5. Conclusion

Modification of the ACP structure with 2.5 wt% of Sr ensures prolonged amorphous phase stability of Sr-ACP in the dry state for at least 3.5 years making it a more feasible component of medical devices compared to pure ACP. Furthermore, the incorporation of Sr-ACP granules improves the subchondral bone formation capacity of a Col/Col-Mg-HAp scaffold in weight-bearing areas during osteochondral defect repair. We propose the use of Sr-ACP granules in the bone layer of a bilayered osteochondral scaffold to enhance osteochondral defect repair.

All authors approved the final version of the manuscript.

Funding

This work was supported by the European Union's Horizon 2020 research and innovation programme [grant numbers EURONANOMED2017-077]; Science Foundation of Ireland [grant Number SFI/16/ENM-ERA/3458]; Ministero della Salute (IMH); Stated Education Development Agency SEDA/VIAA; Technology Foundation (STW). The authors acknowledge financial support from the European Union's Horizon 2020 research and innovation programme under the grant agreement No. 857287 (BBCE – Baltic Biomaterials Centre of Excellence).

CRediT authorship contribution statement

Jietao Xu: Writing – review & editing, Writing – original draft, Investigation, Formal analysis, Data curation. **Jana Vecstaudza:** Writing – review & editing, Writing – original draft, Investigation, Formal analysis, Data curation. **Marinus A. Wesdorp:** Writing – review & editing, Investigation. **Margot Labberté:** Writing – review & editing, Investigation, Data curation. **Nicole Kops:** Writing – review & editing, Investigation. **Manuela Salerno:** Writing – review & editing, Writing – original draft. **Joeri Kok:** Writing – review & editing, Formal analysis, Data curation. **Marina Simon:** Writing – review & editing, Formal analysis, Data curation. **Marie-Françoise Harmand:** Writing – review & editing, Formal analysis, Data curation. **Karin Vancíková:** Writing – review & editing, Investigation. **Bert van Rietbergen:** Writing – review & editing. **Massimiliano Maraglino Misciagna:** Writing – review & editing, Resources. **Laura Dolcini:** Writing – review & editing, Resources. **Giuseppe Filardo:** Writing – review & editing, Project administration, Funding acquisition, Conceptualization. **Eric Farrell:** Writing – review & editing, Supervision, Funding acquisition, Conceptualization. **Gerjo J.V.M. van Osch:** Writing – review & editing, Writing – original draft, Supervision, Project administration, Funding acquisition, Data curation, Conceptualization. **Janis Locs:** Writing – review & editing, Writing – original draft, Project administration, Funding acquisition, Data curation, Conceptualization. **Pieter A.J. Brama:** Writing – review & editing, Writing – original draft, Supervision, Project administration, Investigation, Funding acquisition, Data curation, Conceptualization.

Declaration of competing interest

The authors declare the following financial interests/personal relationships which may be considered as potential competing interests:M. Maraglino Misciagna and L. Dolcini work at Fin-Ceramica Faenza S. p.A, a company that develops, manufactures, and markets collagen/collagen-magnesium-hydroxyapatite scaffolds for orthopaedic and spinal applications.

Data availability

Data will be made available on request.

Acknowledgements

The authors acknowledge Yanto Ridwan for the support in the micro-CT scanning, and Mart Verhoeven and Wouter van de Ven for the support in the micro-CT evaluation. This work was supported through the use of imaging equipment provided bij the Applied Molecular Imaging Erasmus MC facility. The authors acknowledge Christian Poinsot for the support in cytotoxicity assessment.

Appendix A. Supplementary data

Supplementary data to this article can be found online at https://doi.org/10.1016/j.mtbio.2024.100959.

References

[1] J.S. Temenoff, A.G. Mikos, Review: tissue engineering for regeneration of articular cartilage, Biomaterials 21 (5) (2000) 431–440.
[2] J.F. Mano, R.L. Reis, Osteochondral defects: present situation and tissue engineering approaches, Journal of tissue engineering and regenerative medicine 1 (4) (2007) 261–273.
[3] T.M. McCarrel, S.L. Pownder, S. Gilbert, M.F. Koff, E. Castiglione, R.A. Saska, G. Bradica, L.A. Fortier, Two-year evaluation of osteochondral repair with a novel biphasic graft saturated in bone marrow in an equine model, Cartilage 8 (4) (2017) 406–416.
[4] E.E. Mahmoud, N. Kamei, G. Kamei, T. Nakasa, R. Shimizu, Y. Harada, N. Adachi, N.A. Misk, M. Ochi, Role of mesenchymal stem cells densities when injected as suspension in joints with osteochondral defects, Cartilage 10 (1) (2019) 61–69.
[5] P.C. Kreuz, M. Steinwachs, C. Erggelet, S.J. Krause, C. Ossendorf, D. Maier, N. Ghanem, M. Uhl, M. Haag, Classification of graft hypertrophy after autologous chondrocyte implantation of full-thickness chondral defects in the knee, Osteoarthritis Cartilage 15 (12) (2007) 1339–1347.
[6] A.H. Gomoll, H. Madry, G. Knutsen, N. van Dijk, R. Seil, M. Brittberg, E. Kon, The subchondral bone in articular cartilage repair: current problems in the surgical management, Knee surgery, sports traumatology, arthroscopy, official journal of the ESSKA 18 (4) (2010) 434–447.
[7] E. Kon, M. Delcogliano, G. Filardo, M. Fini, G. Giavaresi, S. Francioli, I. Martin, D. Pressato, E. Arcangeli, R. Quarto, M. Sandri, M. Marcacci, Orderly osteochondral regeneration in a sheep model using a novel nano-composite multilayered biomaterial, J. Orthop. Res. 28 (1) (2010) 116–124.
[8] E. Kon, G. Filardo, F. Perdisa, G. Venieri, M. Marcacci, Clinical results of multilayered biomaterials for osteochondral regeneration, J Exp Orthop 1 (1) (2014) 10.
[9] A. Sessa, I. Romandini, L. Andriolo, A. Di Martino, M. Busacca, S. Zaffagnini, G. Filardo, Treatment of juvenile knee osteochondritis dissecans with a cell-free biomimetic osteochondral scaffold: clinical and MRI results at mid-term follow-up, Cartilage 13 (1_suppl) (2021) 1137s–1147s.
[10] X. Xue, Y. Hu, Y. Deng, J. Su, Recent advances in design of functional biocompatible hydrogels for bone tissue engineering, Adv. Funct. Mater. 31 (19) (2021) 2009432.
[11] I. Antonia, V.M. Paltanea, G. Paltanea, A. Antoniac, I.V. Nemoianu, M.I. Petrescu, H. Dura, A.D. Bodog, Additive manufactured magnesium-based scaffolds for tissue engineering, Materials 15 (23) (2022) 8693.
[12] E. Kon, M. Delcogliano, G. Filardo, D. Pressato, M. Busacca, B. Grigolo, G. Desando, M. Marcacci, A novel nano-composite multi-layered biomaterial for treatment of osteochondral lesions: technique note and an early stability pilot clinical trial, Injury 41 (7) (2010) 693–701.
[13] F. Perdisa, G. Filardo, A. Sessa, M. Busacca, S. Zaffagnini, M. Marcacci, E. Kon, One-step treatment for patellar cartilage defects with a cell-free osteochondral scaffold: a prospective clinical and mri evaluation, Am. J. Sports Med. 45 (7) (2017) 1581–1588.
[14] A. Di Martino, F. Perdisa, G. Filardo, M. Busacca, E. Kon, M. Marcacci, S. Zaffagnini, Cell-free biomimetic osteochondral scaffold for the treatment of knee lesions: clinical and imaging results at 10-year follow-up, Am. J. Sports Med. 49 (10) (2021) 2645–2650.
[15] A.A. Dhollander, W.C. Huysse, P.C. Verdonk, K.L. Verstraete, R. Verdonk, G. Verbruggen, K.F. Almqvist, MRI evaluation of a new scaffold-based allogenic chondrocyte implantation for cartilage repair, Eur. J. Radiol. 75 (1) (2010) 72–81.
[16] S. Von Euw, Y. Wang, G. Laurent, C. Drouet, F. Babonneau, N. Nassif, T. Azaïs, Bone mineral: new insights into its chemical composition, Sci. Rep. 9 (1) (2019) 8456.
[17] J.T.B. Ratnayake, M. Mucalo, G.J. Dias, Substituted hydroxyapatites for bone regeneration: a review of current trends, J. Biomed. Mater. Res. B Appl. Biomater. 105 (5) (2017) 1285–1299.
[18] C. Combes, C. Rey, Amorphous calcium phosphates: synthesis, properties and uses in biomaterials, Acta Biomater. 6 (9) (2010) 3362–3378.
[19] S.V. Dorozhkin, Synthetic amorphous calcium phosphates (ACPs): preparation, structure, properties, and biomedical applications, Biomater. Sci. 9 (23) (2021) 7748–7798.
[20] F. Bertolotti, F.J. Carmona, G. Dal Sasso, G.B. Ramírez-Rodríguez, J.M. Delgado-López, J.S. Pedersen, F. Ferri, N. Masciocchi, A. Guagliardi, On the amorphous layer in bone mineral and biomimetic apatite: a combined small- and wide-angle X-ray scattering analysis, Acta Biomater. 120 (2021) 167–180.
[21] L. Degli Esposti, M. Iafisco, Amorphous calcium phosphate, the lack of order is an abundance of possibilities, Biomater Biosyst 5 (2022) 100037.
[22] I. Lodoso-Torrecilla, R. Klein Gunnewiek, E.C. Grosfeld, R.B.M. de Vries, P. Habibović, J.A. Jansen, J. van den Beucken, Bioinorganic supplementation of calcium phosphate-based bone substitutes to improve in vivo performance: a systematic review and meta-analysis of animal studies, Biomater. Sci. 8 (17) (2020) 4792–4809.
[23] B. Wan, R. Wang, Y. Sun, J. Cao, H. Wang, J. Guo, D. Chen, Building osteogenic microenvironments with strontium-substituted calcium phosphate ceramics, Front. Bioeng. Biotechnol. 8 (2020) 591467.
[24] M. Pilmane, K. Salma-Ancane, D. Loca, J. Locs, L. Berzina-Cimdina, Strontium and strontium ranelate: historical review of some of their functions, Mater. Sci. Eng., C 78 (2017) 1222–1230.
[25] S.R. Gavinho, A.S. Pádua, L.I.V. Holz, I. Sá-Nogueira, J.C. Silva, J.P. Borges, M. A. Valente, M.P.F. Graça, Bioactive glasses containing strontium or magnesium ions to enhance the biological response in bone regeneration, Nanomaterials 13 (19) (2023) 2717.
[26] K. ostka, S. Hosseini, M. Epple. In-vitro cell response to strontium/magnesium-doped calcium phosphate nanoparticles, Micro 3 (1) (2023) 156–171.
[27] S. Bose, G. Fielding, S. Tarafder, A. Bandyopadhyay, Understanding of dopant-induced osteogenesis and angiogenesis in calcium phosphate ceramics, Trends Biotechnol. 31 (10) (2013) 594–605.
[28] V.K. Dommeti, S. Roy, S. Pramanik, A. Merdji, A. Ouldyerou, M. Özcan, Design and development of tantalum and strontium ion doped hydroxyapatite composite coating on titanium substrate: structural and human osteoblast-like cell viability studies, Materials 16 (4) (2023) 1499.
[29] M. Schumacher, M. Gelinsky, Strontium modified calcium phosphate cements - approaches towards targeted stimulation of bone turnover, J. Mater. Chem. B 3 (23) (2015) 4626–4640.
[30] M. Jiménez, C. Abradelo, J. San Román, L. Rojo, Bibliographic review on the state of the art of strontium and zinc based regenerative therapies. Recent developments and clinical applications, J. Mater. Chem. B 7 (12) (2019) 1974–1985.
[31] S. Zhang, Y. Dong, M. Chen, Y. Xu, J. Ping, W. Chen, W. Liang, Recent developments in strontium-based biocomposites for bone regeneration, J. Artif. Organs 23 (3) (2020) 191–202.
[32] N. Neves, D. Linhares, G. Costa, C.C. Ribeiro, M.A. Barbosa, In vivo and clinical application of strontium-enriched biomaterials for bone regeneration: a systematic review, Bone Joint Res 6 (6) (2017) 366–375.
[33] J. Vecstaudza, J. Locs, Effect of Synthesis Temperature and Ca/P Ratios on Specific Surface Area of Amorphous Calcium Phosphate, Key Engineering Materials, Trans Tech Publ, 2017, pp. 172–176.
[34] J. Vecstaudza, J. Locs, Novel preparation route of stable amorphous calcium phosphate nanoparticles with high specific surface area, J. Alloys Compd. 700 (2017) 215–222.
[35] J. Vecstaudza, M. Gasik, J. Locs, Amorphous calcium phosphate materials: formation, structure and thermal behaviour, J. Eur. Ceram. Soc. 39 (4) (2019) 1642–1649.
[36] K. Rubenis, S. Zemjane, J. Vecstaudza, J. Bitenieks, J. Locs, Densification of amorphous calcium phosphate using principles of the cold sintering process, J. Eur. Ceram. Soc. 41 (1) (2021) 912–919.
[37] S. Pagani, M. Salerno, G. Filardo, J. Locs, G.J.V.M. van Osch, J. Vecstaudza, L. Dolcini, V. Borsari, M. Fini, G. Giavaresi, M. Columbaro, Human osteoblasts' response to biomaterials for subchondral bone regeneration in standard and aggressive environments, Int. J. Mol. Sci. 24 (19) (2023) 14764.
[38] Z. Cai, Y. Li, W. Song, Y. He, H. Li, X. Liu, Anti-inflammatory and prochondrogenic in situ-formed injectable hydrogel crosslinked by strontium-doped bioglass for cartilage regeneration, ACS Appl. Mater. Interfaces 13 (50) (2021) 59772–59786.
[39] H. Yu, Y. Liu, X. Yang, J. He, F. Zhang, Q. Zhong, X. Guo, Strontium ranelate promotes chondrogenesis through inhibition of the Wnt/β-catenin pathway, Stem Cell Res. Ther. 12 (1) (2021) 296.
[40] J.C. Elliott, Structure and Chemistry of the Apatites and Other Calcium Orthophosphates, 1994.
[41] M.L. de Vries-van Melle, R. Narcisi, N. Kops, W.J. Koevoet, P.K. Bos, J.M. Murphy, J.A. Verhaar, P.M. van der Kraan, G.J. van Osch, Chondrogenesis of mesenchymal stem cells in an osteochondral environment is mediated by the subchondral bone, Tissue engineering, Part. Accel. 20 (1–2) (2014) 23–33.
[42] T.J. Levingstone, A. Ramesh, R.T. Brady, P.A.J. Brama, C. Kearney, J.P. Gleeson, F. J. O'Brien, Cell-free multi-layered collagen-based scaffolds demonstrate layer specific regeneration of functional osteochondral tissue in caprine joints, Biomaterials 87 (2016) 69–81.
[43] D.C. Browe, R. Burdis, P.J. Díaz-Payno, F.E. Freeman, J.M. Nulty, C.T. Buckley, P. A.J. Brama, D.J. Kelly, Promoting endogenous articular cartilage regeneration using extracellular matrix scaffolds, Materials Today Bio 16 (2022) 100343.
[44] R. Burdis, F. Chariyev-Prinz, D.C. Browe, F.E. Freeman, J. Nulty, E.E. McDonnell, K.F. Eichholz, B. Wang, P. Brama, D.J. Kelly, Spatial patterning of phenotypically distinct microtissues to engineer osteochondral grafts for biological joint resurfacing, Biomaterials 289 (2022) 121750.
[45] M. Van den Borne, N. Raijmakers, J. Vanlauwe, J. Victor, S. De Jong, J. Bellemans, D. Saris, International cartilage repair society (ICRS) and oswestry macroscopic cartilage evaluation scores validated for use in autologous chondrocyte implantation (ACI) and microfracture, Osteoarthritis Cartilage 15 (12) (2007) 1397–1402.
[46] L. Goebel, P. Orth, A. Müller, D. Zurakowski, A. Bücker, M. Cucchiarini, D. Pape, H. Madry, Experimental scoring systems for macroscopic articular cartilage repair correlate with the MOCART score assessed by a high-field MRI at 9.4 T–comparative evaluation of five macroscopic scoring systems in a large animal cartilage defect model, Osteoarthritis Cartilage 20 (9) (2012) 1046–1055.
[47] W. Querido, N. Shanas, S. Bookbinder, M.C. Oliveira-Nunes, B. Krynska, N. Pleshko, Fourier transform infrared spectroscopy of developing bone mineral: from amorphous precursor to mature crystal, Analyst 145 (3) (2020) 764–776.
[48] W. Habraken, P. Habibovic, M. Epple, M. Bohner, Calcium phosphates in biomedical applications: materials for the future? Mater. Today 19 (2) (2016) 69–87.
[49] J. Mahamid, A. Sharir, L. Addadi, S. Weiner, Amorphous calcium phosphate is a major component of the forming fin bones of zebrafish: indications for an amorphous precursor phase, Proc Natl Acad Sci U S A 105 (35) (2008) 12748–12753.
[50] C. Combes, C. Rey, Amorphous calcium phosphates: synthesis, properties and uses in biomaterials, Acta Biomater. 6 (9) (2010) 3362–3378.
[51] Y. Gao, W. Weng, K. Cheng, P. Du, G. Shen, G. Han, B. Guan, W. Yan, Preparation, characterization and cytocompatibility of porous ACP/PLLA composites, J. Biomed. Mater. Res. 79 (1) (2006) 193–200.

[52] M. Nagano, T. Nakamura, T. Kokubo, M. Tanahashi, M. Ogawa, Differences of bone bonding ability and degradation behaviour in vivo between amorphous calcium phosphate and highly crystalline hydroxyapatite coating, Biomaterials 17 (18) (1996) 1771–1777.
[53] X. Huang, D. Yang, W. Yan, Z. Shi, J. Feng, Y. Gao, W. Weng, S. Yan, Osteochondral repair using the combination of fibroblast growth factor and amorphous calcium phosphate/poly(L-lactic acid) hybrid materials, Biomaterials 28 (20) (2007) 3091–3100.
[54] M.J. Olszta, X. Cheng, S.S. Jee, R. Kumar, Y.-Y. Kim, M.J. Kaufman, E.P. Douglas, L. B. Gower, Bone structure and formation: a new perspective, Mater. Sci. Eng. R Rep. 58 (3–5) (2007) 77–116.
[55] L.S. Pryor, E. Gage, C.-J. Langevin, F. Herrera, A.D. Breithaupt, C.R. Gordon, A. M. Afifi, J.E. Zins, H. Meltzer, A. Gosman, Review of bone substitutes, Craniomaxillofacial Trauma Reconstr. 2 (3–4) (2009) 151–160.
[56] S.V. Dorozhkin, Calcium orthophosphates (CaPO4): occurrence and properties, Progress in biomaterials 5 (1) (2016) 9–70.
[57] J.P. Gleeson, N.A. Plunkett, F.J. O'Brien, Addition of hydroxyapatite improves stiffness, interconnectivity and osteogenic potential of a highly porous collagen-based scaffold for bone tissue regeneration, Eur. Cell. Mater. 20 (2010) 218–230.
[58] J.B. Vines, D.J. Lim, J.M. Anderson, H.W. Jun, Hydroxyapatite nanoparticle reinforced peptide amphiphile nanomatrix enhances the osteogenic differentiation of mesenchymal stem cells by compositional ratios, Acta Biomater. 8 (11) (2012) 4053–4063.
[59] A. Tampieri, M. Sandri, E. Landi, D. Pressato, S. Francioli, R. Quarto, I. Martin, Design of graded biomimetic osteochondral composite scaffolds, Biomaterials 29 (26) (2008) 3539–3546.
[60] C. Sosio, A. Di Giancamillo, D. Deponti, F. Gervaso, F. Scalera, M. Melato, M. Campagnol, F. Boschetti, A. Nonis, C. Domeneghini, A. Sannino, G.M. Peretti, Osteochondral repair by a novel interconnecting collagen-hydroxyapatite substitute: a large-animal study, Tissue engineering, Part. Accel. 21 (3–4) (2015) 704–715.
[61] T.J. Levingstone, E. Thompson, A. Matsiko, A. Schepens, J.P. Gleeson, F.J. O'Brien, Multi-layered collagen-based scaffolds for osteochondral defect repair in rabbits, Acta Biomater. 32 (2016) 149–160.
[62] M.T. Fulmer, I.C. Ison, C.R. Hankermayer, B.R. Constantz, J. Ross, Measurements of the solubilities and dissolution rates of several hydroxyapatites, Biomaterials 23 (3) (2002) 751–755.
[63] S. Bose, G. Fielding, S. Tarafder, A. Bandyopadhyay, Understanding of dopant-induced osteogenesis and angiogenesis in calcium phosphate ceramics, Trends Biotechnol. 31 (10) (2013) 594–605.
[64] R.P. Radzki, M. Bieńko, R. Filip, Wpływ ranelinianiu strontu na mineralizację i wytrzymałość mechaniczną kości udowej orchidektomizowanych szczurów, Med. Weter. 63 (2007) 163–164.
[65] D. Marx, A. Rahimnejad Yazdi, M. Papini, M. Towler, A review of the latest insights into the mechanism of action of strontium in bone, BoneKEy Rep. 12 (2020) 100273.
[66] B. Kołodziejska, N. Stępień, J. Kolmas, The influence of strontium on bone tissue metabolism and its application in osteoporosis treatment, Int. J. Mol. Sci. 22 (12) (2021) 6564.
[67] Z. Saidak, P.J. Marie, Strontium signaling: molecular mechanisms and therapeutic implications in osteoporosis, Pharmacol. Therapeut. 136 (2) (2012) 216–226.
[68] M.J. Root, Inhibition of the amorphous calcium phosphate phase transformation reaction by polyphosphates and metal ions, Calcif. Tissue Int. 47 (2) (1990) 112–116.
[69] W. Jin, Z. Liu, Y. Wu, B. Jin, C. Shao, X. Xu, R. Tang, H. Pan, Synergic effect of Sr2+ and Mg2+ on the stabilization of amorphous calcium phosphate, Cryst. Growth Des. 18 (10) (2018) 6054–6060.
[70] A.L. Boskey, A.S. Posner, Magnesium stabilization of amorphous calcium phosphate: a kinetic study, Mater. Res. Bull. 9 (7) (1974) 907–916.
[71] N.C. Blumenthal, F. Betts, A.S. Posner, Stabilization of amorphous calcium phosphate by Mg and ATP, Calcif. Tissue Res. 23 (1) (1977) 245–250.
[72] H. Ding, H. Pan, X. Xu, R. Tang, Toward a detailed understanding of magnesium ions on hydroxyapatite crystallization inhibition, Cryst. Growth Des. 14 (2) (2014) 763–769.
[73] M.L. de Vries-van Melle, M.S. Tihaya, N. Kops, W.J. Koevoet, J.M. Murphy, J. A. Verhaar, M. Alini, D. Eglin, G.J. van Osch, Chondrogenic differentiation of human bone marrow-derived mesenchymal stem cells in a simulated osteochondral environment is hydrogel dependent, Eur. Cell. Mater. 27 (2014) 112–123. ; discussion 123.
[74] E. Kon, M. Delcogliano, G. Filardo, M. Busacca, A. Di Martino, M. Marcacci, Novel nano-composite multilayered biomaterial for osteochondral regeneration: a pilot clinical trial, Am. J. Sports Med. 39 (6) (2011) 1180–1190.
[75] E. Kon, A. Muttini, E. Arcangeli, M. Delcogliano, G. Filardo, N. Nicoli Aldini, D. Pressato, R. Quarto, S. Zaffagnini, M. Marcacci, Novel nanostructured scaffold for osteochondral regeneration: pilot study in horses, Journal of tissue engineering and regenerative medicine 4 (4) (2010) 300–308.
[76] S. Davis, M. Roldo, G. Blunn, G. Tozzi, T. Roncada, Influence of the mechanical environment on the regeneration of osteochondral defects, Front. Bioeng. Biotechnol. 9 (2021) 603408.
[77] C.J. van Bergen, G.M. Kerkhoffs, N. Marsidi, C.M. Korstjens, V. Everts, L.J. van Ruijven, C.N. van Dijk, L. Blankevoort, Osteochondral defects of the talus: a novel animal model in the goat, Tissue Eng. C Methods 19 (6) (2013) 449–457.
[78] M. Maglio, S. Brogini, S. Pagani, G. Giavaresi, M. Tschon, Current trends in the evaluation of osteochondral lesion treatments: histology, histomorphometry, and biomechanics in preclinical models, BioMed Res. Int. 2019 (2019) 4040236.
[79] M. Sartori, S. Pagani, A. Ferrari, V. Costa, V. Carina, E. Figallo, M.C. Maltarello, L. Martini, M. Fini, G. Giavaresi, A new bi-layered scaffold for osteochondral tissue regeneration: in vitro and in vivo preclinical investigations, Mater. Sci. Eng., C 70 (2017) 101–111.
[80] B. Grigolo, C. Cavallo, G. Desando, C. Manferdini, G. Lisignoli, A. Ferrari, N. Zini, A. Facchini, Novel nano-composite biomimetic biomaterial allows chondrogenic and osteogenic differentiation of bone marrow concentrate derived cells, J. Mater. Sci. Mater. Med. 26 (2015) 173.
[81] C. Manferdini, C. Cavallo, B. Grigolo, M. Fiorini, A. Nicoletti, E. Gabusi, N. Zini, D. Pressato, A. Facchini, G. Lisignoli, Specific inductive potential of a novel nanocomposite biomimetic biomaterial for osteochondral tissue regeneration, J Tissue Eng Regen Med 10 (2016) 374–391.
[82] C.H. Siebert, O. Miltner, M. Weber, S. Sopka, S. Koch, C. Niedhart, Healing of osteochondral grafts in an ovine model under the influence of bFGF, Arthroscopy 19 (2) (2003) 182–187.